



Environmental  
Science  
Nano

**Transition Metal Doped MgO Nanoparticles for Nutrient Recycling: An Alternate Mg Source for Struvite Synthesis from Wastewater**

Journal:	<i>Environmental Science: Nano</i>
Manuscript ID	EN-ART-06-2020-000660.R1
Article Type:	Paper

SCHOLARONE™  
Manuscripts

## Environmental Significance

High concentrations of phosphorous and nitrogen nutrients in agricultural wastewater leads to eutrophication of water sources which adversely affects aquatic ecosystems and result in greenhouse gas emissions. To sustainably capture and recycle these nutrients to agricultural systems, we studied use of nanostructured MgO as analogs for natural mineral-based Mg sources to produce struvite from wastewater. Undoped and Cu, Fe, and Zn doped nanostructured MgO samples were produced via a facile sol-gel synthesis method. The porosity and high surface area achieved without the use of any support material allowed for enhanced transport of phosphate ions leading to fast struvite formation kinetics for undoped MgO. The addition of transition metals inhibited phosphate adsorption compared to the undoped MgO.

## Transition Metal Doped MgO Nanoparticles for Nutrient Recycling: An Alternate Mg Source for Struvite Synthesis from Wastewater

Manoj Silva,<sup>1</sup> Vadim Murzin,<sup>2,3</sup> Lihua Zhang,<sup>4</sup> John Baltrus,<sup>5</sup> and Jonas Baltrusaitis<sup>1,\*</sup>

<sup>1</sup>Department of Chemical and Biomolecular Engineering, Lehigh University, B336 Iacocca Hall, 111 Research Drive, Bethlehem, PA 18015, USA

<sup>2</sup>Deutsches Elektronen Synchrotron DESY, D-22607 Hamburg, Germany

<sup>3</sup>Bergische Universität Wuppertal, Gaußstraße 20, D-42119, Wuppertal, Germany

<sup>4</sup>Brookhaven National Laboratory, Center for Functional Nanomaterials, Upton, NY 11973, USA

<sup>5</sup>National Energy Technology Laboratory, U.S. Department of Energy, 626 Cochrans Mill Road, Pittsburgh, PA 15236, USA

### Abstract

Nutrient - nitrogen (N) and phosphorus (P) - recovery from wastewater is an important challenge for enhanced environmental sustainability. Herein we report the synthesis and properties of mesoporous MgO nanoparticles doped with copper (Cu), iron (Fe), and zinc (Zn) as an alternative low solubility high abundance magnesium (Mg) source for crystalline struvite precipitation from nutrient-laden wastewater. Undoped MgO was shown to have the fastest phosphate ( $\text{PO}_4^{3-}$ ) adsorption kinetics with a  $k_2$  value of  $0.9 \text{ g g}^{-1} \text{ min}^{-1}$  at room temperature. The corresponding rate constant decreased for Cu-MgO ( $0.175 \text{ g g}^{-1} \text{ min}^{-1}$ ), Zn-MgO ( $0.145 \text{ g g}^{-1} \text{ min}^{-1}$ ), and Fe-MgO ( $0.02 \text{ g g}^{-1} \text{ min}^{-1}$ ). Undoped MgO resulted in the highest  $\text{PO}_4^{3-}$  removal at 94%, while Cu-MgO, Fe-MgO, and Zn-MgO resulted in 90%, 66% and 66%, respectively, under equivalent reaction conditions. All dopants resulted in the production of struvite as the main product with the incorporation of the transition metals into the struvite crystal lattice. X-ray absorption spectroscopy (XAS) showed that the majority of the Cu, Fe, and Zn were primarily in +2, +3, and +2 oxidation states respectively. XAS also showed that the Cu atoms exist in elongated octahedral coordination, while Fe was shown to be in octahedral coordination. Zn was shown to be in a complex disordered environment with octahedral sites co-existing with the majority of tetrahedral sites. Finally, X-ray

1  
2  
3 Photoelectron Spectroscopy data suggest a two-fold struvite surface enrichment with dopant  
4 metals with Cu exhibiting an interesting new local binding structure. The dopant concentrations  
5 utilized were consistent with those found in natural Mg minerals suggesting that (a) utilizing  
6 natural mineral periclase as the Mg source for struvite production can result in struvite formation  
7 albeit at the expense of the reaction kinetics and overall yields while also (b) supplying essential  
8 micronutrients, such as Zn and Cu, necessary for balanced nutrient uptake.  
9  
10  
11  
12  
13  
14  
15  
16  
17  
18  
19  
20

21 \*Corresponding author: [job314@lehigh.edu](mailto:job314@lehigh.edu), phone +1-610-758-6836

22 **Keywords:** MgO;;; adsorption kinetics; struvite; wastewater; nutrients; phosphate  
23  
24  
25  
26  
27  
28  
29  
30  
31  
32  
33  
34  
35  
36  
37  
38  
39  
40  
41  
42  
43  
44  
45  
46  
47  
48  
49  
50  
51  
52  
53  
54  
55  
56  
57  
58  
59  
60

1  
2  
3 **Introduction.** Modern mineral fertilizer have revolutionized agriculture by dramatically  
4 increasing productivity, but have also exhibited detrimental effects on the global nutrient cycles in  
5 the environment.<sup>1-3</sup> Nitrogen (N) fertilizer production requires high energy input and results in net  
6 positive carbon dioxide emissions but up to 90% of the applied N can be lost via either runoff or  
7 greenhouse gas emissions.<sup>2,4</sup> Phosphorous (P) is a mined nutrient and is considered to be used  
8 unsustainably.<sup>5</sup> Both N and P are lost from agricultural systems into the watershed, resulting in  
9 eutrophication that causes greenhouse gas emission, restricting to freshwater, and destruction of  
10 aquatic ecosystems.<sup>6</sup> Capturing nutrients from any wastewater and reusing them in agriculture can  
11 be viewed as an integral part of the circular economy. Nutrient-rich municipal and industrial  
12 wastewater can contain between 100-5000 ppm of total N and up to 1200 ppm of total P.<sup>7</sup> Struvite,  
13  $\text{MgNH}_4\text{PO}_4 \cdot 6\text{H}_2\text{O}$ , crystallization allows for simultaneous removal of  $\text{NH}_4^+$  and  $\text{PO}_4^{3-}$  from  
14 nutrient-laden wastewater by forming a solid fertilizer material. Struvite is a low solubility mineral  
15 ( $\text{pK}_{\text{sp}} = 13.36$ )<sup>8</sup> that exhibits slow-nutrient release properties.<sup>9</sup> Scientific literature on struvite  
16 precipitation from wastewater chiefly focuses on the use of water-soluble magnesium precursor  
17 salts, such as magnesium chloride ( $\text{MgCl}_2$ ).<sup>9,10</sup> However,  $\text{MgCl}_2$  production from seawater or brine  
18 is energy-intensive and renders the struvite precipitation process less environmentally  
19 sustainable.<sup>11,12</sup> Therefore, the use of low-cost and more sustainable Mg sources is desired.

20  
21  
22  
23  
24  
25  
26  
27  
28  
29  
30  
31  
32  
33  
34  
35  
36  
37  
38  
39  
40  
41  
42  
43 The use of earth-abundant low solubility magnesium sources for struvite crystallization such as  
44 periclase ( $\text{MgO}$ )<sup>13-17</sup>, magnesite ( $\text{MgCO}_3$ )<sup>18,19</sup>, brucite ( $\text{Mg}(\text{OH})_2$ )<sup>20</sup>, and dolomite  
45 ( $\text{CaMg}(\text{CO}_3)_2$ )<sup>21-23</sup> has been recently reported in the literature resulting in up to 80%  $\text{NH}_4^+$   
46 removal. These minerals present an abundant and low-cost source of Mg for struvite  
47 precipitation.<sup>13</sup> Importantly, in contrast to using  $\text{MgCl}_2$  where homogeneous nucleation results in  
48 struvite growth, a low solubility magnesium mineral has to undergo a heterogeneous surface  
49  
50  
51  
52  
53  
54  
55  
56  
57  
58  
59  
60

1  
2  
3 reaction leading to struvite crystallization. This results in unique reaction kinetics and growth  
4 mechanisms, as well as the reactive intermediates so far explored to a limited extent.<sup>21</sup> A study  
5 using MgO supported on diatomite<sup>14</sup> investigated the effect of MgO dispersion over a high surface  
6 area substrate and reported faster kinetics than the microcrystalline MgO by the virtue of the  
7 measured higher pseudo-second-order reaction constant.<sup>13</sup> However, the use of mesoporous MgO  
8 without the use of support for struvite crystallization has not been widely reported in the literature.  
9  
10 Another facet of the heterogeneous struvite crystallization problem is the effect of transition metals  
11 commonly present in wastewater. Cu, Fe and Zn are typically present in anthropogenic  
12 wastewater.<sup>24,25</sup> There are only a few studies on their effects on struvite formation kinetics as well  
13 as the complex structure of the resulting struvite.<sup>25-27</sup> For example, the effect of Cu and Zn present  
14 in the solution for struvite formation using MgCl<sub>2</sub> has been reported, as well as the adsorption of  
15 these metal ions on the formed struvite product.<sup>25-29</sup> Using Extended X-Ray Absorption Fine  
16 Structure spectroscopy, EXAFS, Cu was shown to adsorb on the struvite surface in four-fold  
17 coordination while Zn was shown to exist in a mixed coordination environment with more  
18 tetrahedrally coordinated Zn centers.<sup>26</sup> However, the effect on struvite formation kinetics of  
19 transition metals present in the heterogeneous MgO structure has not been studied previously.

20  
21  
22  
23  
24  
25  
26  
27  
28  
29  
30  
31  
32  
33  
34  
35  
36  
37  
38  
39  
40  
41 The current study aims to synthesize nanostructured low solubility MgO nanoparticles for struvite  
42 production to accelerate the underlying reaction kinetics. We report that mesoporous MgO can be  
43 fabricated as a nanostructured material with high surface area and porosity without requiring  
44 support while also allowing fast intraparticle diffusion and faster surface reaction rates due to the  
45 increased number of adsorption sites. Furthermore, the effects of transition metals present in these  
46 model MgO nanoparticles on the kinetics, equilibrium concentrations and product characterization  
47 are presented. Natural Mg minerals contain up to 5% of transition metals such as Cu, Zn, and Fe  
48  
49  
50  
51  
52  
53  
54  
55  
56  
57  
58  
59  
60

1  
2  
3 and thus, utilization of natural Mg minerals or transition metal doped nanomaterials have  
4 significant environmental implications for the global nutrient cycles.<sup>30–33</sup> While previous reports  
5 have theoretically demonstrated that the adsorption properties of the MgO surface change with the  
6 addition of these metals,<sup>34</sup> the effects of these metals under struvite formation conditions have not  
7 been reported previously. Utilization of mesoporous MgO allows for the study of model systems  
8 analogous to natural Mg minerals containing these transition metal impurities. In this work, we  
9 report the use of synthesized mesoporous MgO nanoparticles with Cu, Fe, Zn dopants for struvite  
10 precipitation from simulated wastewater with the objectives of investigating the resulting changes  
11 in reaction kinetics and product characterization.  
12  
13  
14  
15  
16  
17  
18  
19  
20  
21  
22  
23

## 24 **Materials and Methods**

25  
26  
27 **Synthesis of MgO nanoparticles (MgO NPs).** MgO NPs were prepared by a modified method  
28 previously reported.<sup>35</sup> An 8.7 mM Mg(NO<sub>3</sub>)<sub>2</sub> solution was prepared by adding Mg(NO<sub>3</sub>)<sub>2</sub>·6H<sub>2</sub>O  
29 (MilliporeSigma, 99%) to methanol and heated until reflux temperature was achieved. A 17.4 mM  
30 NaOH solution was prepared in methanol and added dropwise to the Mg(NO<sub>3</sub>)<sub>2</sub> solution. After  
31 thirty minutes of reaction at reflux temperature, the precipitate was collected by centrifugation,  
32 washed three times using a 1:1 ratio of ethanol/water solution, and dried at 80 °C overnight. The  
33 dry solid was then calcined at 450 °C for 2 hours (2 °C/min ramp rate) in static air. Then 0.5 g of  
34 MgO NPs prepared was mixed in 40 ml deionized water and stirred for 12 hours. After stirring,  
35 the gel was separated and dried at 80 °C. The sample was then calcined as described earlier to  
36 obtain the final MgO NPs. Cu-MgO, Fe-MgO, and Zn-MgO samples were prepared via the same  
37 method by adding the appropriate metal nitrate with the Mg(NO<sub>3</sub>)<sub>2</sub>·6H<sub>2</sub>O. The metal nitrates used  
38 for the synthesis were copper(II) nitrate trihydrate (MilliporeSigma, 99%), iron(III) nitrate  
39 nonahydrate (Acros, 98% ACS Reagent), and zinc(II) nitrate hexahydrate (MilliporeSigma, 99%).  
40  
41  
42  
43  
44  
45  
46  
47  
48  
49  
50  
51  
52  
53  
54  
55  
56  
57  
58  
59  
60

1  
2  
3 **Struvite synthesis.** Simulated  $\text{NH}_4^+$  and  $\text{PO}_4^{3-}$  containing wastewater samples were prepared by  
4 adding 600 ppm of monoammonium phosphate,  $\text{NH}_4\text{H}_2\text{PO}_4$  (MAP, 99.9 %, Fisher Scientific) in  
5  
6 18.2 M $\Omega$ /cm deionized water (Millipore, USA). A 600 ppm MAP solution represents  $\text{PO}_4^{3-}$  and  
7  
8  $\text{NH}_4^+$  values found in municipal, animal and industrial wastewater<sup>7</sup> while maintaining above the  
9  
10 molar 1:1 ratio needed for struvite formation. MgO NPs or microcrystalline MgO was added to  
11  
12 500 mL of the simulated wastewater and stirred for up to 120 minutes. Aliquots of 1 mL were  
13  
14 sampled periodically, filtered through a 0.22  $\mu\text{m}$  polyethersulfone filter, and analyzed using ion  
15  
16 chromatography. The MgO concentrations used for struvite synthesis were 100, 300 and 1000  
17  
18 ppm, which correspond to molar  $[\text{Mg}^{2+}]:[\text{NH}_4^+]:[\text{PO}_4^{3-}]$  ratios of 0.48:1:1, 1.44:1:1, and 4.8:1:1.  
19  
20  $[\text{Mg}^{2+}]:[\text{NH}_4^+]:[\text{PO}_4^{3-}]$  ratios of 0.5-1.5:1:1 have previously been tested and was concluded that  
21  
22 lower ratios lead to a lesser N and P adsorption/reaction.<sup>36,37,38,10,39</sup> Therefore, a slight excess of  
23  
24  $\text{Mg}^{2+}$  was preferred in the previous works to circumvent this issue and ensure efficient removal of  
25  
26 N and P from the solution.<sup>10,39</sup> The microcrystalline MgO (MilliporeSigma, 99.9%) was used  
27  
28 without further treatment.  
29  
30  
31  
32  
33  
34  
35

36 **MgO nanoparticle and struvite product characterization.** The crystalline nature of all reactants  
37  
38 and products was confirmed using powder X-ray diffraction (Empyrean, PANalytical B.V.). The  
39  
40 applied current was 40 mA and the applied voltage was 45 kV. The X-ray mirror that was used  
41  
42 was a graded, flat Bragg-Brentano HD mirror, with the step size set to 0.0131 degrees. Nitrogen  
43  
44 physisorption was used to measure surface area using a Micromeritics ASAP2020 surface area and  
45  
46 porosimetry system. High-angle annular dark-field scanning transmission electron microscopy  
47  
48 and energy-dispersive X-ray spectroscopy, high-resolution transmission electron microscopy  
49  
50 (HAADF-STEM EDS and HR-TEM) were used to confirm bulk dopant distribution. HR-TEM  
51  
52 imaging was performed on JEOL2100F operating at 200kV. HAADF-STEM EDS measurements  
53  
54  
55  
56  
57  
58  
59  
60

1  
2  
3 were performed using a Scanning Transmission Electron Microscope (STEM) (FEI Talos 200x)  
4 equipped with a four-quadrant 0.9-sr spectrometer for elemental and compositional mapping.  
5  
6 Perkin-Elmer AAnalyst200 atomic absorption spectrometer (AAS) was utilized with an air-  
7  
8 acetylene flame to measure transition metal concentrations in aqueous solutions. X-ray  
9  
10 photoelectron spectroscopy (XPS) analysis was carried out with a ULVAC-PHI VersaProbe III  
11  
12 instrument using a monochromatized Al K $\alpha$  X-ray source (1486.6 eV). The pass energy of the  
13  
14 analyzer was 55.5 eV, the acquisition area had a diameter of 100  $\mu$ m, and the scan step size was  
15  
16 0.1 eV. Binding energies were corrected for charging by referencing to the C 1s peak at 285.0 eV.  
17  
18 Atomic concentrations were calculated from the areas under individual high-resolution XPS  
19  
20 spectra using manufacturer-provided sensitivity factors. A Metrohm Eco 925 ion chromatography  
21  
22 system (Herisau, Switzerland) was used to measure all aqueous ion concentrations. Separation  
23  
24 columns used were Metrosep A supp 4/5 Guard column (5 $\times$ 4mm), Metrosep A supp 5 (4 $\times$ 150  
25  
26 mm) for anion analysis and Metrosep C 4 Guard column (5 $\times$ 4mm), and Metrosep C 4 (4 $\times$ 150 mm)  
27  
28 for cation analysis. A solution of 1.75 mM HNO<sub>3</sub> and 0.7 mM dipicolinic acid was used as eluent  
29  
30 for Metrosep C 4 while a solution of 3.2 mM Na<sub>2</sub>CO<sub>3</sub> and 1.0 mM NaHCO<sub>3</sub> was used for Metrosep  
31  
32 A supp 5 with a 0.2 M H<sub>2</sub>SO<sub>4</sub> and 0.1 M H<sub>2</sub>C<sub>2</sub>O<sub>4</sub> suppression solution. All samples were measured  
33  
34 at room temperature. MagIC Net 3.2 software was used to control the instrument and process the  
35  
36 chromatograms.  
37  
38  
39  
40  
41  
42  
43  
44

45 X-ray Absorption Near Edge Spectroscopy (XANES) and Extended X-ray Absorption Fine  
46  
47 Structure (EXAFS) measurements were performed at the Advanced X-ray Absorption  
48  
49 Spectroscopy Beamline P64 (PETRA III ring, DESY, Hamburg). Samples were mixed with  
50  
51 microcrystalline cellulose and pressed into powder pellets. Spectra were measured at room  
52  
53 temperature in continuous acquisition mode when the undulator and the monochromator  
54  
55  
56  
57  
58  
59  
60

1  
2  
3 movements were synchronized on the fly. Three ionization chambers were filled with pure  
4 nitrogen to reduce sensitivity to higher harmonics of the undulator. For each set of samples, the  
5 corresponding metal foil (Fe, Cu, Zn) was used as a standard between the second and the third  
6 ionization chambers. The monochromatic beam flux on the sample was ca.  $5 \times 10^{12}$  photons/s. The  
7 time for each spectrum was set to 5 minutes, an average of 3-4 scans was used for the analysis.  
8 Experimental EXAFS spectra were fitted using IFEFFIT and LARCH packages.<sup>40,41</sup> In the fitting  
9 procedure *ab initio* photoelectron backscattering amplitudes and phases were calculated self-  
10 consistently using FEFF8.5 code.<sup>42</sup> EXAFS functions were  $k^2$  and  $k^3$  – weighted and fitted in 1.0-  
11 3.0 Å interval of R-space. The range of photoelectron wave vectors used in the fit was 3.0–15.0  
12 Å<sup>-1</sup>. The amplitude reduction factor  $S_0^2$  was obtained from the fit of the first shell of the  
13 corresponding standard (0.73 for Fe, 0.87 for Cu, 0.85 for Zn). Coordination numbers were fixed,  
14 different models with different coordination numbers were tested, the best model and fit were  
15 taken. Debye-Waller factors,  $\sigma^2$ , distances, R, and the total energy shift,  $\Delta E_0$ , were varied during  
16 the fit.

17  
18  
19  
20  
21  
22  
23  
24  
25  
26  
27  
28  
29  
30  
31  
32  
33  
34  
35  
36 **PO<sub>4</sub><sup>3-</sup> adsorption kinetics and diffusion studies.** The pseudo-second order<sup>43</sup> kinetic model were  
37 used to analyze the obtained PO<sub>4</sub><sup>3-</sup> adsorption data. The linear form of the pseudo-second order  
38 model can be expressed as (1),  
39  
40

$$41 \quad t/q_t = 1/k_2q_e^2 + t/q_e \quad (1)$$

42  
43  
44  
45  
46 where  $q_t$  (mg g<sup>-1</sup>) and  $q_e$  (mg g<sup>-1</sup>) are the amounts of PO<sub>4</sub><sup>3-</sup> adsorbed at time  $t$  (min) and at  
47 equilibrium, respectively.  $k_2$  (g mg<sup>-1</sup> min<sup>-1</sup>) is the rate constant of the pseudo second order kinetic  
48 model. The error bars are based on three independent measurements for each data point. To assess  
49 intraparticle diffusion effects the Weber and Morris model was used<sup>44</sup> and expressed as (2)  
50  
51  
52  
53  
54  
55  
56  
57  
58  
59  
60

$$q_t = k_p t^{0.5} + C \quad (2)$$

where  $k_p$  ( $\text{mg g}^{-1} \text{min}^{-0.5}$ ) is the intraparticle diffusion coefficient and  $C$  is a fitting constant.

## Results and Discussion

### MgO NP Bulk Characterization

**pXRD of MgO NPs.** The synthesized undoped and doped MgO nanoparticles were analyzed using pXRD to confirm the MgO crystal structure. Figure 1(a) shows the pXRD results for all precursor MgO nanoparticles. In all nanoparticles, the MgO pattern was in agreement with the reference pattern of MgO.<sup>45</sup> Powder XRD patterns for the doped MgO NPs showed no new peaks as dopants were introduced at 5% by weight (AAS confirmed dopant concentrations to be as follows: Cu – 4.5%, Fe – 3.8%, Zn – 4.5%). This suggests that either all dopants exist as a solid solution in the MgO cubic crystal structure by replacing  $\text{Mg}^{2+}$  or the nanoparticles formed are under the detection limit of XRD.<sup>46</sup> Upon close examination of the peak of highest intensity which corresponds to the (2 0 0) plane of the MgO structure shown in Figure 1(b), it is observed that the  $2\theta$  positions exhibit slight shifts as Cu and Zn are introduced compared to the undoped MgO. This shift suggests that the Cu and Zn have been successfully added to the parent MgO structure and exist in solid solution rather than forming distinct nanoparticles. The Fe-MgO (2 0 0) peak did not show a significant shift from the MgO pattern. Therefore, Fe must exist in oxide nanoparticle form (< 3nm size crystals) rather than a solid solution.

**Nitrogen Physisorption.** Nitrogen physisorption and application of the Brunauer-Emmett-Teller equation were utilized to measure surface area. Figure 1(c)-(f) show the BET isotherms.

Table 1. BET Surface area for undoped and doped MgO

<b>Sample Name</b>	<b>BET area (m<sup>2</sup>/g)</b>	<b>Pore volume (cm<sup>3</sup>/g)</b>
MgO	177	0.481
Cu-MgO	174	0.630
Fe-MgO	171	0.523
Zn-MgO	174	0.296
Microcrystalline MgO	94	0.219

The introduction of dopants did not significantly alter the BET surface area of the nanoparticles. Examination of the isotherms leads to the conclusion that all particles exhibit mesoporosity. Type IV isotherms are observed with the H3 hysteresis loop for all four NPs.<sup>47</sup> The pore size distributions are shown in Figure S1.

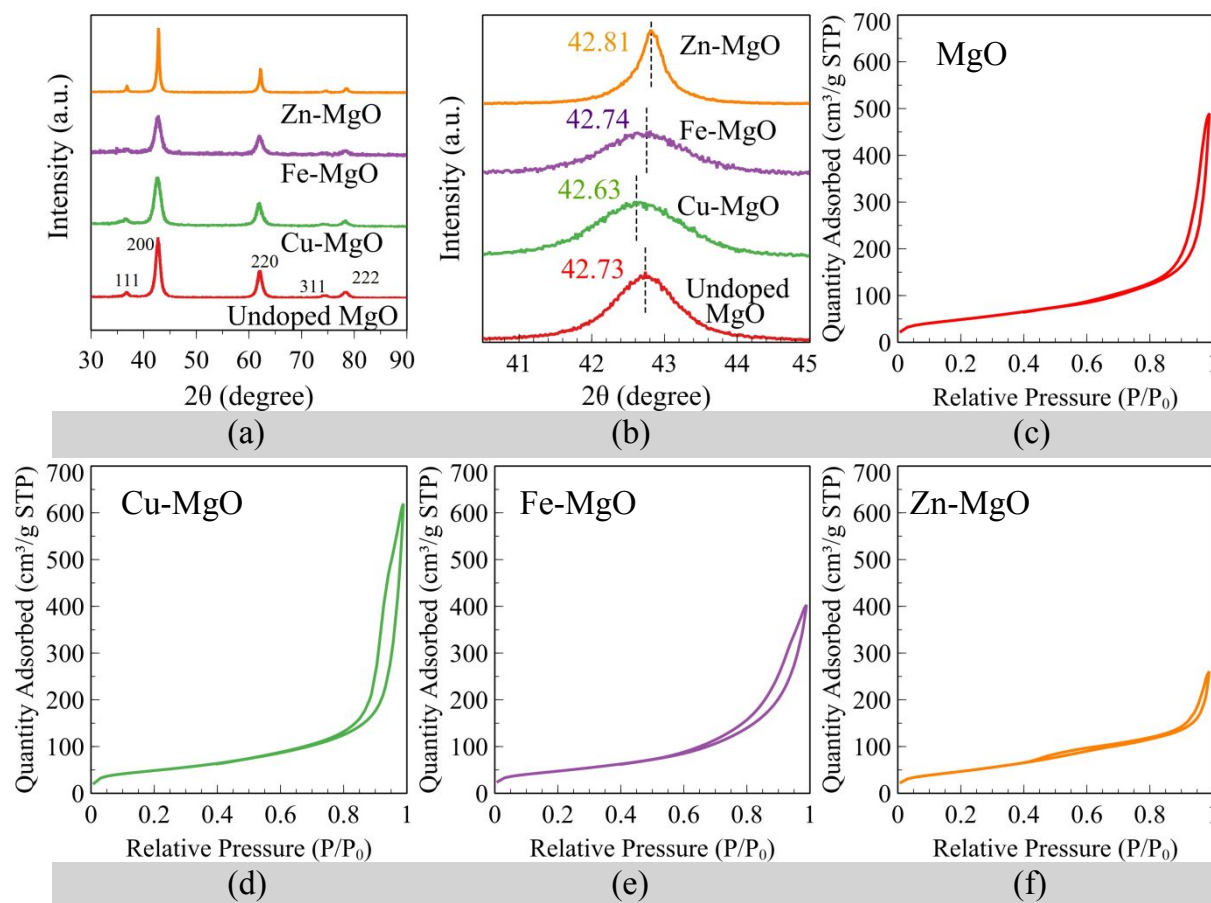
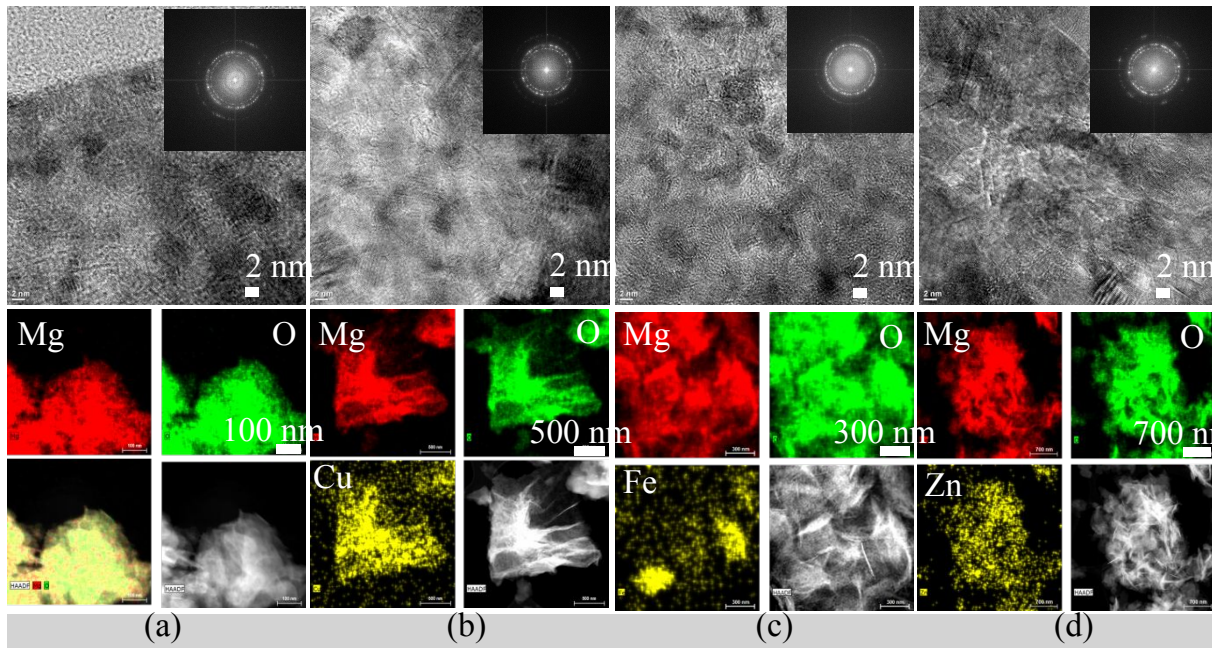


Figure 1. (a) pXRD patterns for MgO NPs. (b) Zoomed in pXRD peak corresponding to MgO (200) in all MgO NPs. BET isotherms for MgO NPs (c) undoped MgO (d) Cu-MgO (e) Fe-MgO (f) Zn-MgO

**HAADF-STEM/EDS and HR-TEM of MgO NPs.** HAADF-STEM/EDS was utilized to confirm dopant distribution and to analyze elemental composition. Figure 2 shows the images for each precursor, along with Fast Fourier Transforms (FFT) of HR-TEM. The STEM/EDS shows in Figure 2(f) and (h) that Cu and Zn are dispersed and there are no distinct nanoparticles of dopant oxides forming. The ring pattern seen by FFT of the HR-TEM images bears similarity to other MgO nanostructures documented in the literature.<sup>48–50</sup> The FFT patterns shown in Figure 2(i)–(l) insets display no new rings or distortions for any of the dopants, confirming that doping does not

1  
2  
3 form large crystals of new oxide phases, but rather confirms that the dopant is introduced into the  
4 same crystal structure at MgO by replacing Mg. The STEM imaging shows that the nanoparticles  
5 do not have a monodisperse distinct morphology, but rather exist in rod-like disordered shapes.  
6  
7  
8  
9  
10 The EDS image of Fe-MgO shows that some Fe is dispersed, but also displays agglomeration  
11 pointing toward sub 3 nm oxide nanoparticle formation. Given the lack of peak shift in XRD, it  
12 can be concluded that while some small amount of Fe may form a solid solution, the majority of  
13  
14  
15  
16  
17  
18  
19 the Fe exists in oxide form as small crystals.



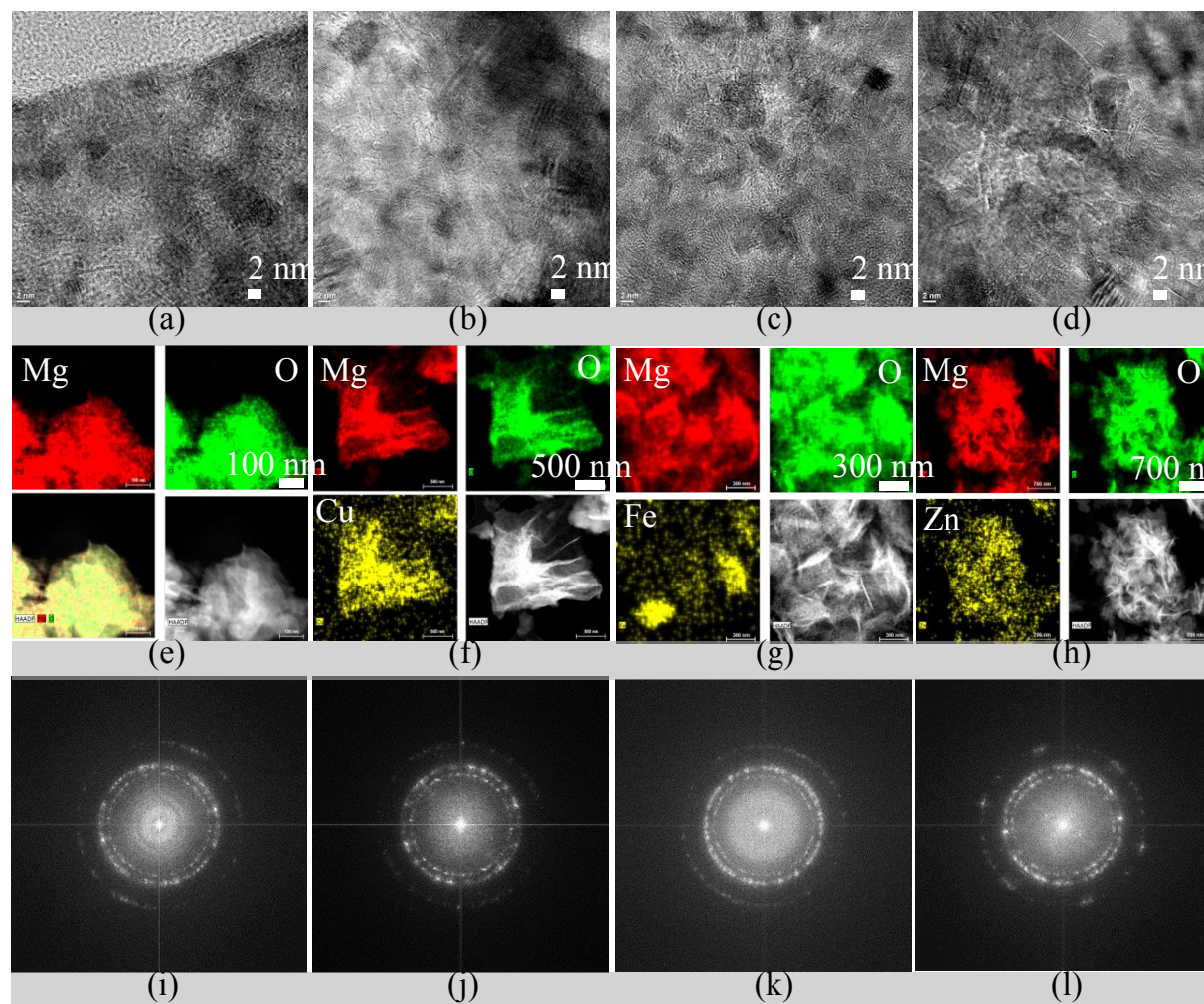


Figure 2. HAADF-STEM EDS and HR-TEM of MgO NPs. (a)-(d) HR-TEM of MgO NPs (e)-(h) HAADF-STEM EDS maps of MgO NPs (i)-(l) Fast Fourier transform of the HR-TEM images of MgO NPs

### MgO NPs Surface Region Characterization

**XPS of MgO NPs.** XPS was utilized to study the chemical state of dopant metals in the surface region of the doped MgO NPs. The resulting Zn 2p<sub>3/2</sub>, Cu 2p, and Fe 2p spectra are shown in Figures 3(a)-(c). Zn 2p<sub>3/2</sub> peak was measured at 1022.0 eV, consistent with the values of low Zn/Mg=0.01 ratio in co-precipitated Zn/MgO and pure ZnO.<sup>51,52</sup> The Cu 2p core level spectrum

exhibits two major peaks centered at binding energies of 934.4 and 954.0 eV, attributed to Cu 2p<sub>3/2</sub> and Cu 2p<sub>1/2</sub> doublets characteristic of copper(II) oxide.<sup>53</sup> This argument is also supported by clear shake-up peaks present at around 942.8 and 962.5 eV. Cu 2p<sub>3/2</sub> has been reported previously at 933.7 eV for a Cu/Mg = 0.01 system prepared via similar chemistry and is consistent with CuO in MgO.<sup>53</sup> Two peaks were observed in the Fe2p region with the apparent peaks at 712.0 and 726.2 eV due to the Fe<sub>2</sub>O<sub>3</sub>. However, previous reports have also documented FeOOH at 711.9 eV and the possibility of the presence of a minor quantity of this species cannot be ruled out.<sup>54</sup> A previous study has reported the presence of a peak higher than 725 eV which shows that the presence of FeOOH is a possibility but, all Fe exists in +3 oxidation state.<sup>55</sup>

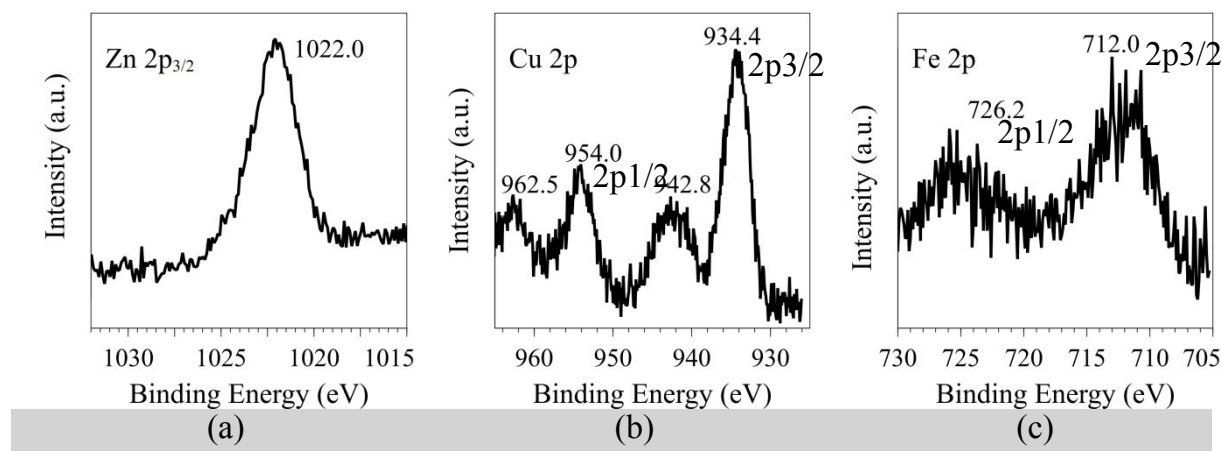


Figure 3. High resolution XPS spectra for MgO NPs. (a) Zn 2p<sub>3/2</sub> (b) Cu 2p (c) Fe 2p.

Atomic surface region composition, as inferred from XPS measurements, is shown in Table 2 in the form of the ratio between the corresponding metal and magnesium concentration. Approximately 5% of the surface region is comprised of the corresponding metal atoms. This agrees with the bulk composition of the dopants determined using AAS measurements.

Table 2. Surface composition of the MgO NPs as the ratio of the metal dopant 2p transition to the respective Mg 2p

Sample Identifier	Zn2p <sub>3/2</sub> /Mg2p	Cu2p/Mg2p	Fe2p/Mg2p
Cu-MgO	-	0.06	-
Fe-MgO	-	-	0.05
Zn-MgO	0.06	-	-

## MgO NP Bulk Electronic and Molecular Structure Characterization

**K-edge XAS of transition metal-doped MgO NPs.** Ambient K-edge XANES analysis was performed to elucidate the geometry and oxidation state of the dopant transition metal ions in the doped MgO and struvite. The Cu-MgO XANES spectrum is plotted with the reference spectra in Figure 4(a). The Cu-MgO shows a minor feature at 8977 eV which is assigned to the 1s → 3d transition (also present in CuSO<sub>4(aq)</sub>).<sup>56,57</sup> The white line position is 8996 eV (consistent with CuO and CuSO<sub>4(aq)</sub>) indicating that majority of the Cu is in +2 oxidation state.<sup>58,59</sup> The lack of a pre-edge indicates that the geometry is not that of Cu<sub>2</sub>O (which displays the pre-edge), but is consistent with CuO and CuSO<sub>4(aq)</sub> in elongated octahedral (Jahn-Teller distortion). CuO exhibits a clear shoulder at 8986 eV, while Cu-MgO has a weak shoulder at 8987 eV. This shoulder is assigned to 1s → 4p transition.<sup>60</sup> The Fe-MgO XANES spectrum is plotted with the reference spectra in Figure 4(b). The Fe-MgO minor pre-edge occurs at 7114 eV while the white line aligns at 7133 eV, both in agreement with Fe<sub>2</sub>O<sub>3</sub> as well as previous reports.<sup>61–63</sup> Previous work done on Fe doped MgO has shown that Fe<sup>3+</sup> can exist in Fe<sub>2</sub>MgO<sub>4</sub> spinel structure, inverse spinel, and as a solid solution within MgO structure.<sup>58</sup> Given the lack of peak shift in pXRD, it is more likely that nanoclusters are the prevalent structure containing the majority of the Fe. Therefore, it can be concluded that Fe is in Fe<sup>3+</sup> octahedrally coordinated with possible Fe<sub>2</sub>MgO<sub>4</sub> spinel nanoclusters or Fe<sub>2</sub>O<sub>3</sub> nanoclusters. The XANES spectra for ZnO and Zn-MgO are plotted in Figure 4(c). Analysis of Zn-MgO shows that Zn-MgO lacks a 9662 eV peak that would evidence any reduced Zn in the sample, thus confirming that all Zn is fully oxidized as shown in previous reports (indicating no

1  
2  
3 empty d states).<sup>57,64</sup> The white line peak at 9670 eV for Zn-MgO is assigned to  $1s \rightarrow 4p$ , while  
4  
5 the splitting of the feature can be attributed to Zn being present in a rigid environment.<sup>65-67</sup> The  
6  
7 broad feature centered around 9680 eV is attributed to multiple scattering resonance and the  
8  
9 decreased intensity of the scattering peak compared to the reference tetrahedral ZnO peak is  
10  
11 indicative of octahedral sites being present due to Zn substitution into the MgO lattice.<sup>65</sup> Therefore,  
12  
13 it can be concluded that Zn local structure differs from that of the tetrahedral structure as in ZnO  
14  
15 to some extent.  
16  
17  
18  
19

20 EXAFS analysis was conducted to elucidate details on Metal-Oxygen (Me-O) and Metal-Metal  
21  
22 (Me-Me) bond length calculation via fitting to theoretical models. Table S2 shows the coordination  
23  
24 numbers used, as well as the bond lengths ( $\text{\AA}$ ) and the Debye-Waller factor,  $\sigma^2$  ( $\text{\AA}^2$ ) values. The  
25  
26 R-space FT-EXAFS spectrum for Cu-MgO is shown in Figure 4(e). The details for the model Cu-  
27  
28 MgO center is shown in Figure S2. The Cu-Cu and Cu-Mg bond lengths are very close in size and  
29  
30 thus, the system is assumed to be highly disordered with a Cu and Mg mixed the second shell that  
31  
32 is difficult to resolve. However, given the Cu dispersion evident from STEM and solid solution  
33  
34 formation indicated by XRD peak shift, the model best fitted here assumed Mg coordinated in the  
35  
36 second sphere. As shown in Table S2, the Cu-O (eq.) bond length is 2.03  $\text{\AA}$  and the Cu-O (ax.)  
37  
38 bond distance is 2.31  $\text{\AA}$ . This is in agreement with previous reports.<sup>68</sup> The EXAFS spectrum in  
39  
40 Figure 4(e) for Fe-MgO shows the Fe-O bond length to be 1.95  $\text{\AA}$  and the Fe-Me bond length to  
41  
42 be 2.98  $\text{\AA}$ . The second shell was chosen to be Fe-Mg in the simulation but is expected to be a mix  
43  
44 of Fe-Fe and Fe-Mg given that both models result in acceptable fits. The Zn-MgO EXAFS analysis  
45  
46 was done to calculate the Zn-O and Zn-Mg bond lengths, which were found to be 2.12  $\text{\AA}$  and 3.00  
47  
48  $\text{\AA}$ . The Zn-Mg path fit required an N=12 value, similar to some work done in a previous report.<sup>57</sup>  
49  
50 The deviations of the experimental data from the theoretical EXAFS curves show that the Zn-MgO  
51  
52  
53  
54  
55  
56  
57  
58  
59  
60

system is highly disordered. As shown by XANES analysis, given the suspected mixture of coordination environments for Zn the disorder may cause the complex EXAFS spectrum.

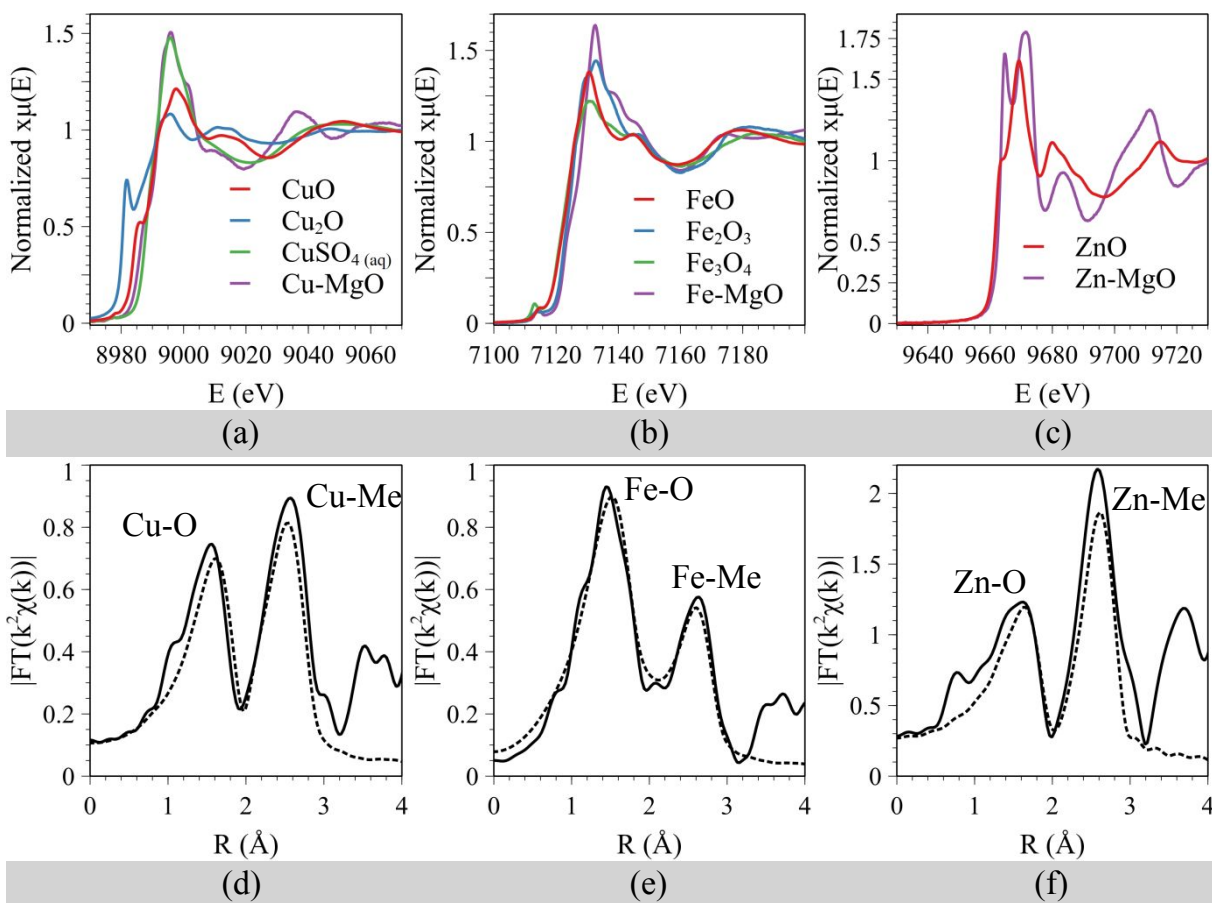


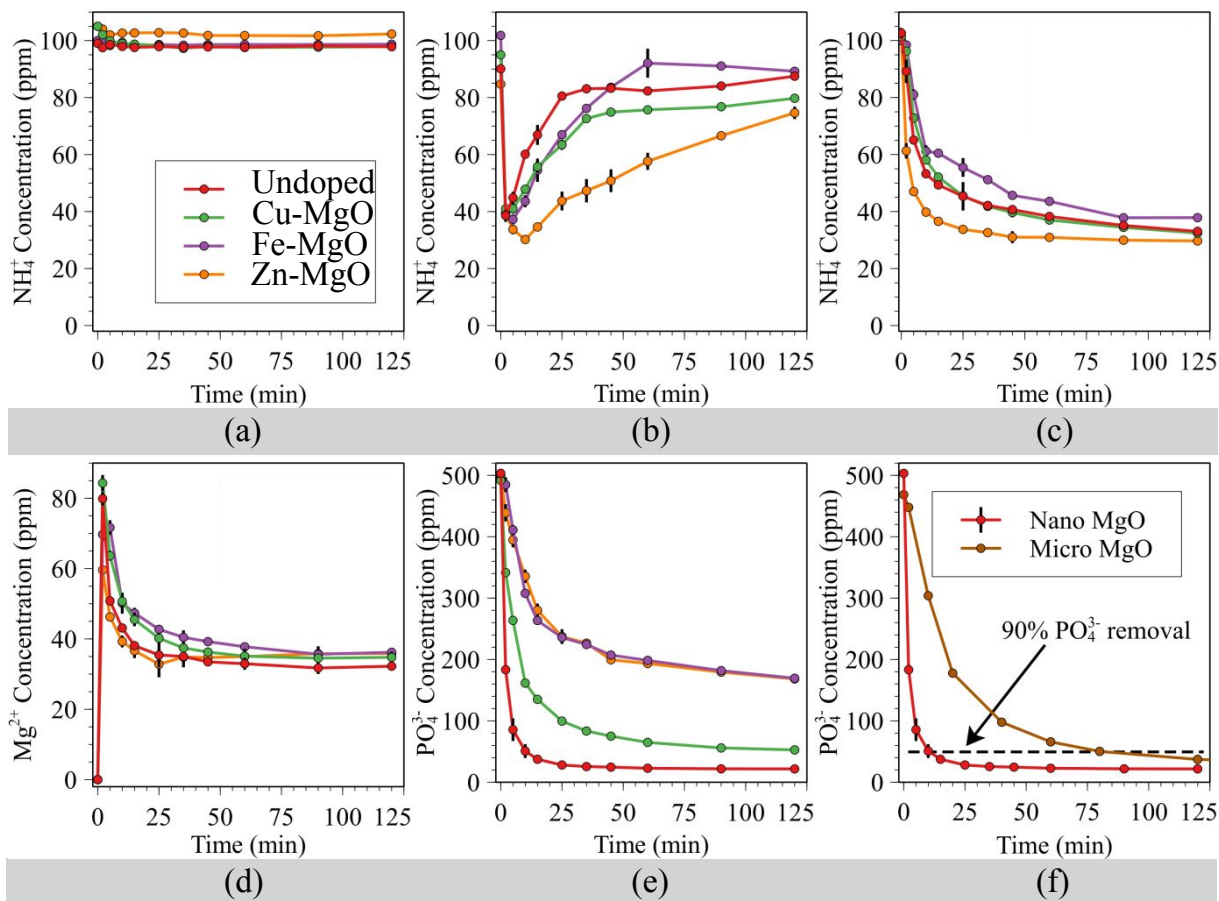
Figure 4. Ambient K-edge XANES spectra including reference oxide standards for (a) Cu-MgO (b) Fe-MgO (c) Zn-MgO. Ambient K-edge FT EXAFS experimental spectra without phase shift corrections (solid line) and best-fitting model spectra (dashed line) (d) Cu-MgO (e) Fe-MgO (f) Zn-MgO.

### Phosphate Adsorption Kinetics and Ion Chromatography Studies

IC was utilized to measure  $Mg^{2+}$ ,  $NH_4^+$ , and  $PO_4^{3-}$  ion concentrations over the 120 minute reaction time for batch experiments conducted at 25°C. As shown in Figure 5(a) at 100 ppm MgO loading, no adsorption of  $NH_4^+$  was observed. This could be attributed to the low  $Mg^{2+}$  concentration not

1  
2  
3 reaching the supersaturation threshold. Figure 5(b) shows the 1000 ppm MgO loading. Here the  
4  $\text{Mg}^{2+}:\text{NH}_4^+:\text{PO}_4^{3-}$  molar ratio is 4.8:1:1 and thus, supersaturation is well above the limit required  
5  
6 for struvite crystallization. For comparison, the 1000 ppm microcrystalline MgO loading has been  
7  
8 reported to have a transient effect on  $\text{NH}_4^+$  adsorption<sup>13</sup> and this same behavior was observed here  
9  
10 for nanostructured MgO. The 1000 ppm MgO NP loading was shown to adsorb  $\text{NH}_4^+$  in the initial  
11  
12 2-10 min time but later released the  $\text{NH}_4^+$  ions back into the solution. While the mechanistic details  
13  
14 for the transient  $\text{NH}_4^+$  adsorption are unclear, one hypothesis to explain this behavior could be that  
15  
16 the increased MgO loading increases supersaturation well beyond the struvite formation limit to  
17  
18 form  $\text{Mg}_3(\text{PO}_4)_2 \cdot 22\text{H}_2\text{O}$ . Figure 5(c) shows  $\text{NH}_4^+$  concentration as a function of time for the 300  
19  
20 ppm loading of MgO NPs. This was identified to be the optimal loading to produce struvite as the  
21  
22 major product since all higher loadings produced other magnesium phosphate phases as the  
23  
24 primary product and did not produce struvite. All  $\text{PO}_4^{3-}$  adsorption studies were conducted at the  
25  
26 300 ppm loading. Figure 5(d) shows the  $\text{Mg}^{2+}$  concentration in the solution as a function of time  
27  
28 for the 300 ppm loading. The final concentration of  $\text{Mg}^{2+}$  in the solution after the total reaction  
29  
30 time of 120 minutes is within the 32-36 ppm range for all MgO NPs. Figure 5(e) shows the  $\text{PO}_4^{3-}$   
31  
32 concentration in the solution as a function of time. The undoped MgO showed the fastest kinetics  
33  
34 of adsorption at 25°C with 90%  $\text{PO}_4^{3-}$  adsorbed after 10 minutes of reaction and 94% adsorption  
35  
36 after the total reaction time of 120 minutes. Cu-MgO resulted in 90% adsorption, while both Fe-  
37  
38 MgO and Zn-MgO lead to 66% adsorption. Adding dopants exhibited lower reaction rates and  
39  
40 equilibrium adsorbed  $\text{PO}_4^{3-}$  values compared to the undoped MgO. Finally, the undoped MgO was  
41  
42 compared to the microcrystalline MgO as shown in Figure 5(f). Remarkably, the undoped MgO  
43  
44 NPs achieve 90%  $\text{PO}_4^{3-}$  adsorption after 10 minutes, while the microcrystalline MgO requires 80  
45  
46 minutes. The faster adsorption performance shows that the nanostructured undoped MgO can act  
47  
48  
49  
50  
51  
52  
53  
54  
55  
56  
57  
58  
59  
60

as a more efficient  $\text{PO}_4^{3-}$  adsorbent compared to the microcrystalline MgO. The increased surface area and porosity of the nanostructured MgO (as shown in Table 1) are expected to facilitate rapid diffusion in the initial time range.



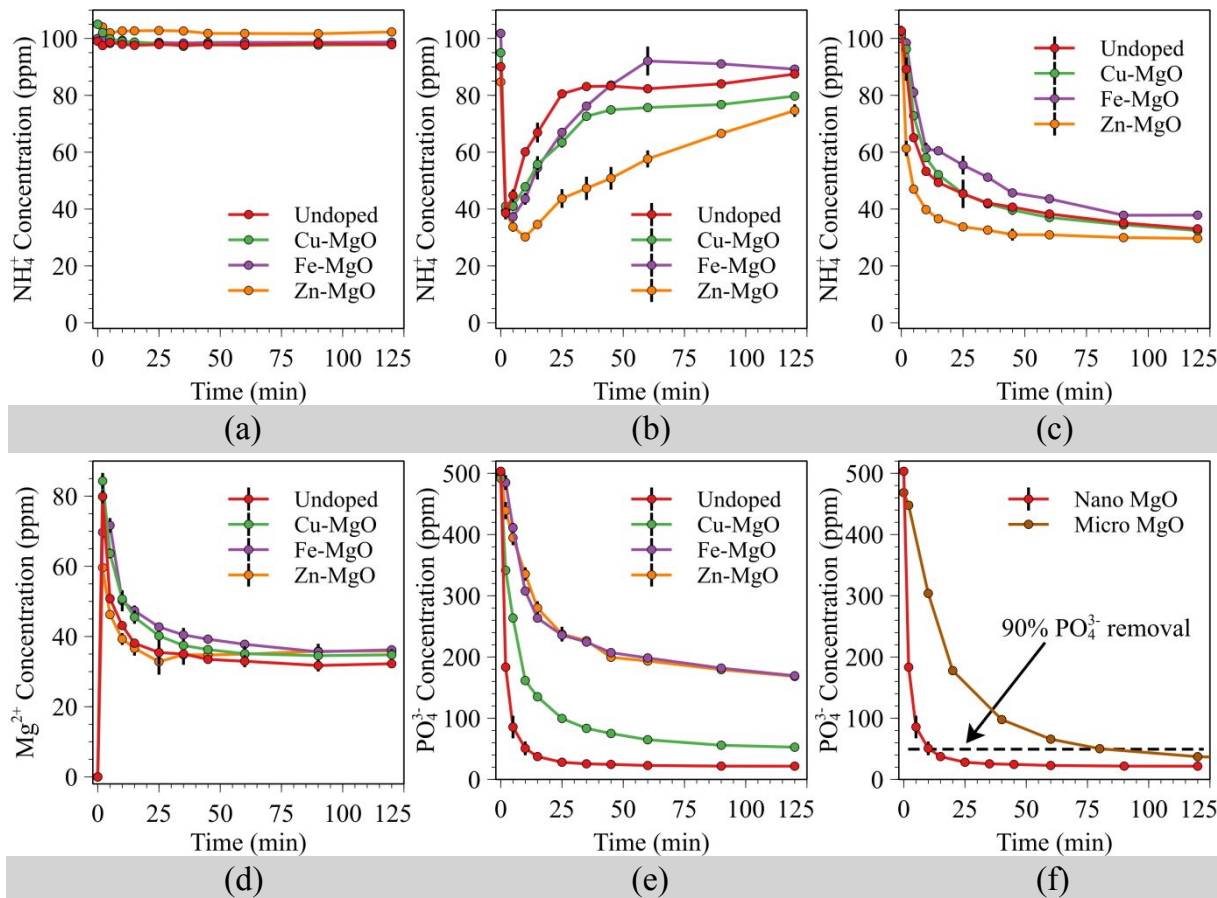


Figure 5. Ion chromatography measurements obtained at 25°C for undoped and doped MgO (a)  $\text{NH}_4^+$  concentration for 100 ppm MgO (b)  $\text{NH}_4^+$  concentration for 1000 ppm MgO (c)  $\text{NH}_4^+$  concentration for 300 ppm MgO (d)  $\text{Mg}^{2+}$  concentration for 300 ppm MgO (e)  $\text{PO}_4^{3-}$  concentration for 300 ppm MgO. (f)  $\text{PO}_4^{3-}$  concentrations recorded over time for undoped nano MgO and microcrystalline MgO. The dashed line shows the 90%  $\text{PO}_4^{3-}$  adsorption point for each species. Error bars represent the standard deviation for experiments performed in duplicate.

The pseudo-second order kinetic model and the Weber and Morris model for intraparticle diffusion were used to fit the phosphate concentration profiles between 0-35 min and 0-5 min time ranges. Table S1 contains all the kinetic parameters calculated using the two models. The pseudo-second order rate constant  $k_2$  was used to compare the reaction kinetics for each MgO material. The rate

1  
2  
3 constants calculated from the pseudo-second order model are apparent rate constants and not  
4  
5 intrinsic rate constants for phosphate adsorption or struvite formation. The 0-35 min time range  
6  
7 was used since all MgO NPs are close to equilibrium after this time range. As shown in Table S1,  
8  
9 undoped MgO shows the highest  $k_2$  value at 25°C with  $9.00 \times 10^{-4} \text{ g mg}^{-1} \text{ min}^{-1}$ . Cu-MgO results in  
10  
11 a  $k_2$  value of  $1.75 \times 10^{-4} \text{ g mg}^{-1} \text{ min}^{-1}$  for the pseudo-second order model. Both undoped MgO and  
12  
13 Cu-MgO fit the pseudo-second order model with high  $R^2$  values ( $R^2 > 0.99$ ). However, the Fe-MgO  
14  
15 and Zn-MgO data did not fit the pseudo-second order model with acceptable  $R^2$  values. The  
16  
17 pseudo-second order was chosen specifically since previous work on phosphate adsorption on  
18  
19 MgO reported the use of the pseudo-second order model.<sup>13,14</sup> The pseudo-first order model is not  
20  
21 applicable for this system since the theoretical work done on pseudo-first order model derivation  
22  
23 has shown that it provides physically meaningful information only for systems where the adsorbate  
24  
25 concentration in the aqueous phase does not significantly change.<sup>69,70</sup> Therefore, only the use of  
26  
27 the pseudo-second order model is discussed in this report. In the temperature range of 25°C - 45°C,  
28  
29 both undoped MgO and Cu-MgO fit the pseudo-second order model with high  $R^2$  values, while  
30  
31 Fe-MgO and Zn-MgO showed poor fits.  
32  
33  
34  
35  
36  
37

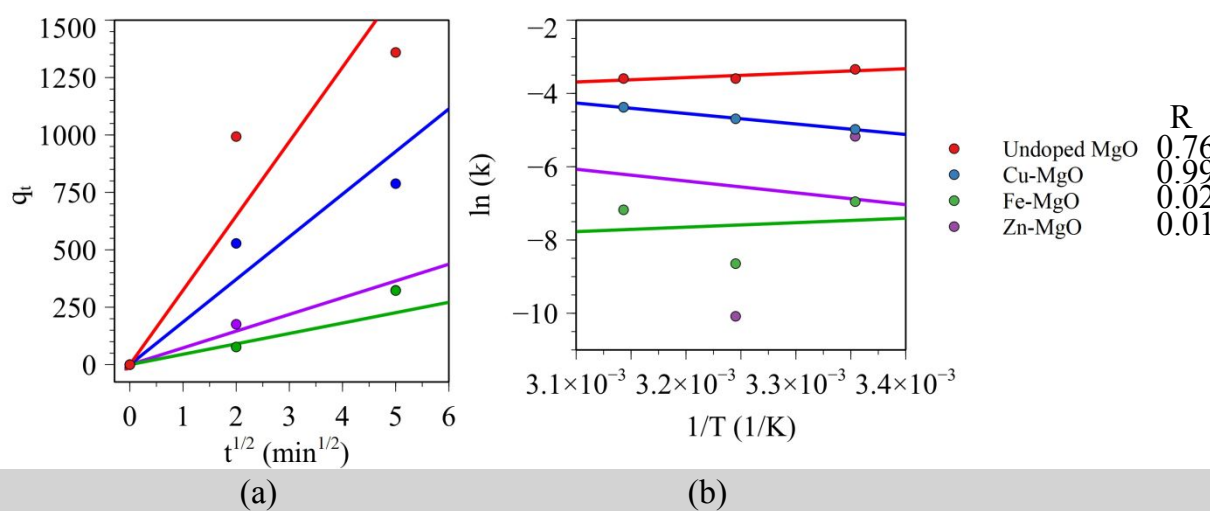
38 The 0-5 min time range was used to assess initial reaction kinetics. As shown in Table S1, undoped  
39  
40 MgO data fit the pseudo-second order model with acceptable  $R^2$  value in this time range. However,  
41  
42 doped MgO NPs did not fit the pseudo-second order model in the initial 0-5 min time range as  
43  
44 denoted by the low  $R^2$  values. A close examination of the phosphate adsorption curves in Figure  
45  
46 5(e) shows that undoped MgO displays a two-regime behavior; the fast initial adsorption from 0-  
47  
48 5 minutes, and the slower adsorption approaching equilibrium from 10-35 minutes. The doped  
49  
50 MgO NPs did not result in this two-regime behavior. Previous studies have shown that the surface  
51  
52 of MgO undergoes significant structural changes, as well as the configurational entropic effects of  
53  
54  
55  
56  
57  
58  
59  
60

1  
2  
3 the phosphate and hydrogen phosphate chain formation necessary for adsorption.<sup>21</sup> This complex  
4 surface transformation is not necessarily well described by generalized pseudo-order models.  
5  
6 Therefore, the pseudo-order results are mainly used to describe a trend in performance, rather than  
7  
8 to elucidate absolute values.  
9  
10

11  
12  
13 The intraparticle diffusion effects are considered by modeling the initial  $\text{PO}_4^{3-}$  adsorption using  
14 the Weber and Morris equation.<sup>44</sup> The intraparticle diffusion model was used to analyze the  
15 phosphate adsorption data as shown by Figure 6(a). Table 4 contains all intraparticle diffusion  
16 coefficient ( $k_p$ ) values and the C parameter values calculated using phosphate adsorption data at  
17  
18 25°C. The C parameter in the Weber and Morris equation denotes whether the surface reaction  
19 effects or diffusion effects dominate the adsorption process, with the C-values indicating that  
20  
21 diffusion is not the only dominant process and that surface adsorption is also playing a role in the  
22 rate-limiting step.<sup>71</sup> The diffusion effects become important in comparing the initial adsorption  
23 kinetics during the 0-5 minute time range where undoped MgO displays significantly faster  
24 kinetics, while Fe-MgO and Zn-MgO both display comparatively slower adsorption. The undoped  
25 MgO  $k_p$  was over four times the values of Fe-MgO and Zn-MgO while it exceeded 1.5 times the  
26 value of Cu-MgO. This fast diffusion may be seen as one of the reasons for the fast adsorption  
27 during the initial 5 minutes of reaction for undoped MgO. Microcrystalline MgO data fits with  
28 acceptable accuracy to show a  $k_p$  value of  $177.43 \text{ mg g}^{-1} \text{ min}^{-0.5}$  compared to the  $618.25 \text{ mg g}^{-1}$   
29  $\text{min}^{-0.5}$  value of undoped MgO, which once again proves the increased efficiency advantage of  
30  
31 nanomaterials. The increased surface area and mesoporosity allow for more favorable transport  
32 properties in the nanomaterial.  
33  
34  
35  
36  
37  
38  
39  
40  
41  
42  
43  
44  
45  
46  
47  
48  
49  
50

51  
52  
53 The apparent rate constant  $k_2$  values for 25°C, 35°C, and 45°C were used to construct Arrhenius  
54 plots for each MgO NP species to calculate apparent activation energies. The Arrhenius plots for  
55  
56  
57

the undoped and doped MgO NPs are shown by Figure 6(b) with the  $R^2$  values for each sample. The  $k_2$  values calculated from undoped MgO lead to an  $R^2$  value of 0.766 and a positive slope which is not physically meaningful. This leads to the conclusion that the apparent rate constants calculated for undoped MgO are mathematically significant but, the physical meaning lacks the mechanistic insights of surface restructuring to form the correct adsorption site for phosphate. The two-regime behavior seen in undoped MgO is not in agreement with the pseudo-second order model, which shows that some modification to existing adsorption models is required to elucidate a physically meaningful rate constant. The Arrhenius plot for Cu-MgO shown in Figure 6(b) fits with a high  $R^2$  value. The apparent activation energy calculated from the slope was 23.8 kJ/mol. Given that the  $R^2$  values for both the pseudo-second-order plots and the Arrhenius plots are high for Cu-MgO, the model predicted  $k_2$  value can be physically meaningful. Conversely, Fe-MgO and Zn-MgO data are poorly fitted to the pseudo-second-order model (as discussed previously) and therefore, the  $k_2$  values did not yield a good fit to the Arrhenius equation. Therefore, it was not possible to calculate apparent activation energies for Fe-MgO and Zn-MgO using the pseudo-order models.



1  
2  
3 Figure 6. (a) Intra-particle diffusion model fits for MgO NPs (b) Arrhenius plots for MgO NPs  
4 with  $R^2$  values.  
5  
6  
7

### 8 **Struvite Product Bulk Characterization**

9

10  
11 **pXRD characterization of products.** The products formed from the 2-hour reaction with 300  
12 ppm loadings of MgO NPs were characterized using pXRD. All samples exhibit patterns in  
13 agreement with struvite reference PDF#15-0762 as shown in Figure 7. No unreacted MgO peaks  
14 are present in the pXRD patterns, indicating that all MgO was fully converted. For undoped  
15 struvite and Cu-struvite, a minor peak at  $11^\circ$  (denoted with \*) is observed. This peak is due to the  
16 presence of a small fraction of  $\text{Mg}_3(\text{PO}_4)_2 \cdot 22\text{H}_2\text{O}$  (PDF#35-0186). The  $\text{PO}_4^{3-}$  adsorption in each  
17 case is slightly above 1:1 ratio compared to  $\text{NH}_4^+$  adsorption. This slight excess  $\text{PO}_4^{3-}$  removal is  
18 due to the formation of  $\text{Mg}_3(\text{PO}_4)_2 \cdot 22\text{H}_2\text{O}$ . The mass fraction of  $\text{Mg}_3(\text{PO}_4)_2 \cdot 22\text{H}_2\text{O}$  in the case of  
19 undoped struvite production was calculated to be around 6.9% of the total product assuming that  
20 struvite and  $\text{Mg}_3(\text{PO}_4)_2 \cdot 22\text{H}_2\text{O}$  are the only products. In the cases of Fe-struvite and Zn-struvite,  
21 no distinct phosphate or oxide phases are identified in the pXRD pattern, proving that the dominant  
22 crystalline product is struvite. The mass fractions of Cu, Fe, and Zn in the products were 1.0%,  
23 1.2%, and 1.4%, respectively, as measured by AAS. While Fe content in struvite is not currently  
24 regulated by European Union or the Environmental Protection Agency (EPA), the Cu and Zn  
25 content are regulated to be 200 ppm and 600 ppm, respectively, by the EU, and 3750 ppm and  
26 2000 ppm, respectively, by the EPA.<sup>72,73</sup> Given that the Cu, Fe, and Zn content for struvite formed  
27 using doped MgO exceed these limits, it is important to note that the doped struvites should be  
28 utilized after mixing with undoped struvite to meet the regulation limits and to supply the required  
29 amount of Cu, Fe, and Zn to the soil without overfertilization of micronutrients.  
30  
31  
32  
33  
34  
35  
36  
37  
38  
39  
40  
41  
42  
43  
44  
45  
46  
47  
48  
49  
50  
51  
52  
53  
54  
55  
56  
57  
58  
59  
60

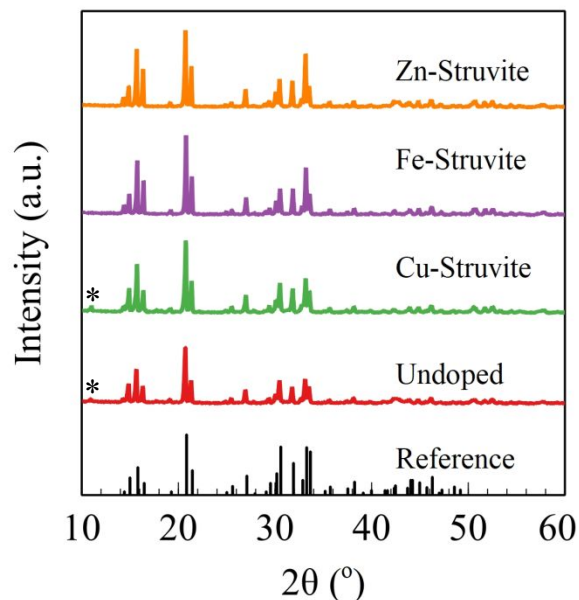


Figure 7. pXRD patterns for products after 2 hour reaction time (Struvite reference PDF#15-0762).

### Struvite Surface Region Characterization.

Figure 8 presents the XPS spectra for the reacted MgO NP products. The Zn  $2p_{3/2}$  spectrum for Zn-struvite in Figure 8(a) shows a peak at 1022.4 eV, which is consistent with literature reports for  $Zn^{2+}$  in ZnO.<sup>74</sup> Figure 8(b) for Cu-struvite shows the Cu  $2p_{3/2}$  peak at 932.6 eV, which has been reported in the literature as  $Cu_2O$  while also overlapping with metallic Cu.<sup>75</sup> The presence of metallic Cu is highly unlikely since XAS results discussed later on in the report do not indicate any presence of metallic Cu. Cu coordinated to various nitrogen ligands have been documented to have binding energies that are close to the observed 932.6 eV<sup>76</sup> suggesting a unique binding environment of Cu. The Fe  $2p_{3/2}$  peak shown in Figure 8(c) exhibits a broad peak centered at 711.1 eV. This suggests that, in addition to the  $Fe_2O_3$  form of  $Fe^{3+}$ , another iron atom binding configuration is likely to be present. Fe  $2p_{3/2}$  peak for  $FePO_4$  was reported at 714.65 eV<sup>77</sup>, similar to that in  $Fe_3(PO_4)_2$ .<sup>78</sup> This shift to higher binding energies is associated with the high electronegativity of phosphate ions. The data shown in Figure 7 for Fe  $2p_{3/2}$  (and

likely for Cu 2p<sub>3/2</sub> peaks) suggest that in the surface region dopants exhibit an opposite behavior, e.g. they are coordinated in a manner where the electron density is not removed from the metal nuclei. Finally, the N 1s peak is present at 401.7 eV with the corresponding P 2p peak at 133.8 eV, suggesting the surface region contains both elements specific to struvite.

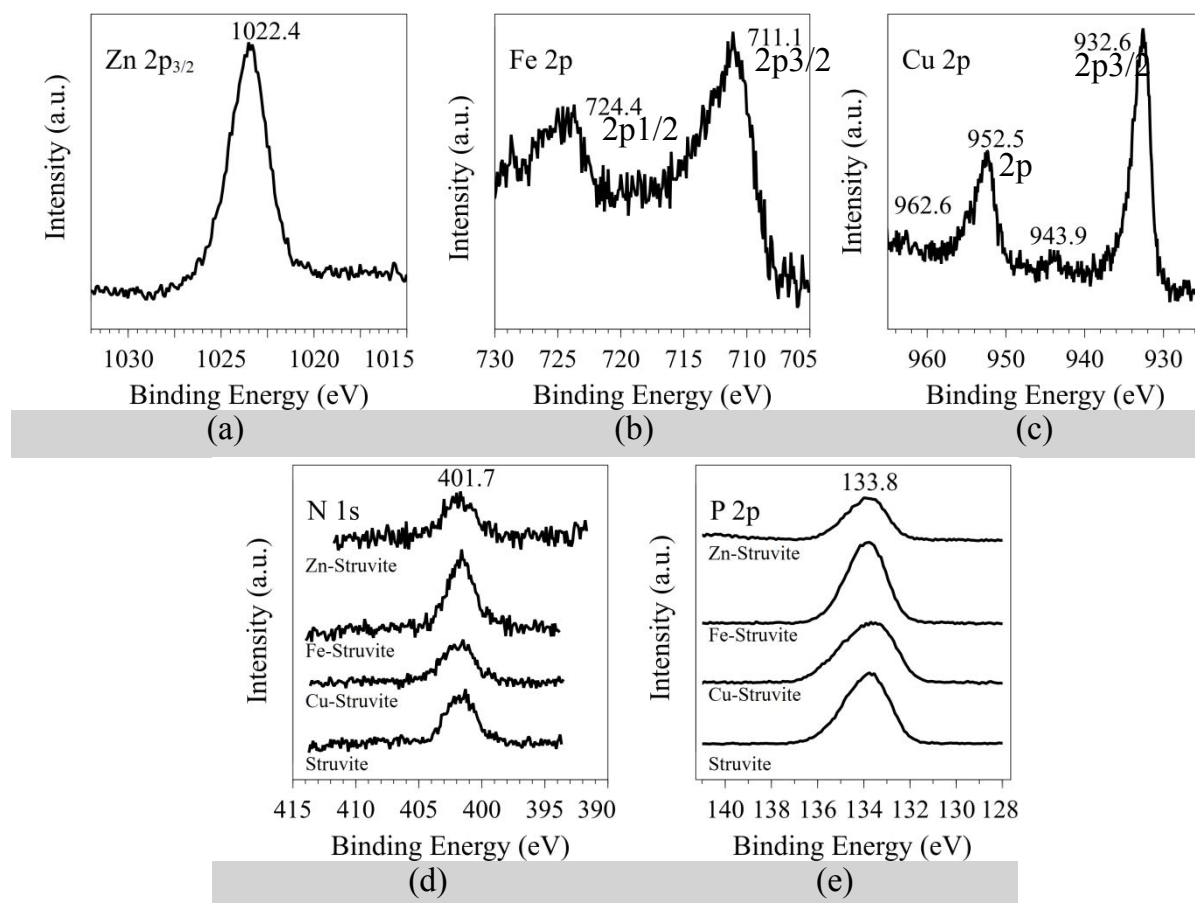


Figure 8. XPS spectra for reacted MgO NP products. (a) Zn 2p<sub>3/2</sub> spectrum (b) Fe 2p spectrum (c) Cu 2p spectrum (d) N 1s spectra (e) P 2p spectra.

The corresponding quantification of the dopants in the surface region is shown in Table 3. The surface region becomes enriched in dopants when compared with the corresponding MgO samples. In particular, a 1.9 to 2.7 increase in the concentration of the dopants is observed per Mg atom. An interesting observation can be made from N/Mg and P/Mg quantification in terms of the

corresponding area under the peak shown in Table 3. The struvite surface region is N-deficient and in some cases, such as Zn-struvite, P-deficient even though the bulk crystallography shown in Figure 7 corresponds to that of struvite. The P/Mg atomic ratio, on the other hand, approached that stoichiometric of struvite of 1.

Table 3. Surface region composition of the reacted MgO NP products as the ratio of the area under the peak of the metal dopant 2p transition peak to the respective Mg 2p peak. An increase in the corresponding ratio from the corresponding doped MgO sample is shown in parenthesis.

Sample Identifier	Cu/Mg (Cu-struvite :Cu-MgO)	Fe/Mg (Fe- struvite:Fe- MgO)	Zn/Mg (Zn- struvite:Zn- MgO)	N/Mg	P/Mg
Struvite	-	-	-	0.19	0.85
Cu-Struvite	0.12 (1.9)	-	-	0.23	0.95
Fe-Struvite	-	0.13 (2.7)	-	0.22	0.98
Zn-Struvite	-	-	0.11 (2.0)	0.08	0.32

### Struvite Product Electronic and Molecular Structure Characterization

**K-edge XAS characterization of products.** The Cu-struvite Cu K-edge XANES spectrum is shown in Figure 9(a) with reference spectra. No pre-edge is observed for Cu-struvite (similar to  $\text{CuSO}_4(\text{aq})$ ) compared to the pre-edge feature seen in the  $\text{Cu}_2\text{O}$  spectrum, indicating elongated octahedral symmetry. The Cu-struvite main edge at 8996 eV aligns within 0.5 eV of the  $\text{CuSO}_4(\text{aq})$  main edge. The agreement with  $\text{CuSO}_4(\text{aq})$  indicates that the majority of the Cu in Cu-struvite exists in elongated octahedral coordination. The white line for Cu-struvite occurs at 8996.4 eV, compared to CuO at 8997.7 eV and  $\text{Cu}_2\text{O}$  at 8995.7 eV. This indicates that a minor fraction of Cu in the Cu-struvite may be reduced as suggested by XPS results. The Fe-struvite spectrum is shown in Figure 9(b) with the reference spectra. The Fe-struvite pre-edge feature occurs at 7114 eV with the main

1  
2  
3 edge occurring at 7133 eV. This shows close alignment with the  $\text{Fe}_2\text{O}_3$  spectrum, indicating that  
4 the majority of Fe in octahedral coordination, similar to Fe-MgO. The Zn-struvite XANES  
5 spectrum is shown in Figure 9(c) with the ZnO reference spectrum. Similar to Zn-MgO, Zn-  
6 struvite shows a split main feature and the scattering resonance peak. This provides evidence for  
7 Zn local structure in Zn-struvite differing significantly from the tetrahedral ZnO structure.  
8  
9

10  
11  
12 The ambient K-edge EXAFS spectrum for Cu-struvite is as shown in Figure 9(d). The absence of  
13 a second shell indicates highly isolated Cu species coordinated to oxygen. The equatorial Cu-O  
14 bond and axial Cu-O distances were calculated to be 1.96 Å and 2.3 Å, while the Cu-Me bond  
15 distance was shown to be 2.96 Å. The Cu-O bond length and Cu-Cu bond lengths previously  
16 reported in a similar Cu-MgO system were 1.96 Å and 3.08 Å, while a standard CuO was reported  
17 to have a Cu-O distance of 1.95 Å.<sup>57,68</sup> The model chosen in this study shows good agreement with  
18 these literature values. The Fe-struvite EXAFS spectrum is shown in Figure 9(e). The EXAFS  
19 displayed the Fe-O and Fe-Me shells, which were fitted to a model with N=6 for the Fe-O path  
20 and N=2 for the Fe-Me path. The Fe-O bond length was calculated to be 1.95 Å and the Fe-Me  
21 bond length was calculated to be 2.98 Å. The second shell is expected to be a mixed Fe-Mg and  
22 Fe-Fe shell given the close bond lengths to Mg-Mg. The Zn-struvite EXAFS spectrum indicates a  
23 disordered system, leading to higher mean-square disorder values (shown in Table S2). The Zn-O  
24 bond distance was calculated to be 1.98 Å and the Zn-Me bond distance was calculated to be 2.95  
25 Å. The Zn-Me bond length is shorter than the previous report for a Zn-MgO system.<sup>57</sup> The EXAFS  
26 analysis of struvites shows that the dopants incorporate in a variety of coordinations, with Cu  
27 showing highly isolated sites but Zn leading toward a highly disordered system with mixed  
28 coordinations.  
29  
30  
31  
32  
33  
34  
35  
36  
37  
38  
39  
40  
41  
42  
43  
44  
45  
46  
47  
48  
49  
50  
51  
52  
53  
54  
55  
56  
57  
58  
59  
60

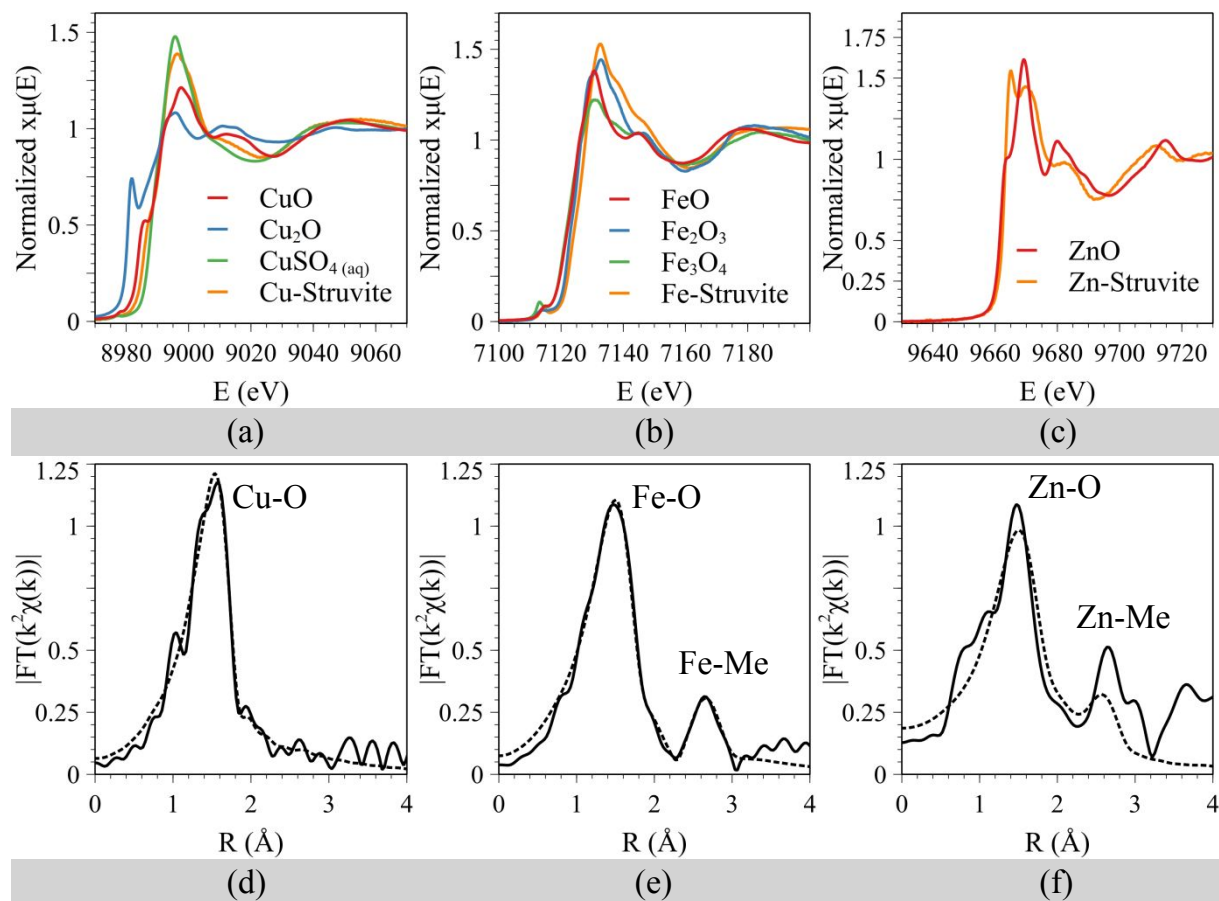


Figure 9. K-edge XANES spectra for struvite products with reference spectra (a) Cu-struvite (b) Fe-struvite (c) Zn-struvite. Ambient K-edge FT EXAFS experimental spectra without phase shift corrections (solid line) and best-fitting model spectra (dashed line) for struvite products (d) Cu-struvite (e) Fe-struvite (f) Zn struvite

**Conclusions.** In summary, we utilized mesoporous transition metal-doped MgO nanoparticles for nutrient recycling via struvite synthesis from simulated wastewater. By enhancing transport properties via increased surface area and porosity, the nano MgO significantly outperforms the microcrystalline MgO. The undoped MgO was shown to be the best performing adsorbent (94% PO<sub>4</sub><sup>3-</sup> removal) while doped MgO NPs resulted in lower  $k_2$  and  $q_e$  values, showing that dopants have an inhibitory effect on PO<sub>4</sub><sup>3-</sup> adsorption. Understanding the chemical properties of metal ions

1  
2  
3 incorporated into the MgO precursor and the struvite product is of importance in assessing whether  
4 natural MgO (which contains metal impurities) can be utilized as a sustainable Mg source for  
5 producing struvite that can be applied to agricultural systems within safety regulations imposed on  
6 fertilizer material. This study demonstrates that critical micronutrients for plant growth can be  
7 incorporated into the slow-release fertilizer struvite during synthesis from wastewater using  
8 transition metal-doped MgO (summarized in Figure S3), which can act as an analog to naturally  
9 occurring insoluble Mg minerals (e.g. periclase) with common transition metal impurities. All  
10 three dopants used in this study were micronutrients relevant to plant growth.<sup>79,80</sup> Zinc, in  
11 particular, is an important micronutrient to be added to soil given the Zn deficiency in US soil.<sup>81</sup>  
12 Incorporating Cu, Fe, and Zn in a slow-release fertilizer allows for controlled release over a long  
13 time since plants uptake micronutrients at a much slower rate compared to macronutrients such as  
14 N and P.<sup>82</sup>

15  
16  
17  
18  
19  
20  
21  
22  
23  
24  
25  
26  
27  
28  
29  
30  
31 **Author Contributions.** V.M. acquired and analyzed XAS data. L.Z. performed microscopy  
32 studies. J.B. acquired XPS data. M.S. conducted experimental design, XRD, and IC. M.S. and J.B.  
33 wrote the manuscript.

34  
35  
36  
37  
38  
39 Manoj Silva - [orcid.org/0000-0002-5353-006X](https://orcid.org/0000-0002-5353-006X)

40  
41  
42 Vadim Murzin – <https://orcid.org/0000-0003-2743-8398>

43  
44  
45 John Baltrus - <http://orcid.org/0000-0003-3253-9193>

46  
47  
48 Jonas Baltrusaitis - [orcid.org/0000-0001-5634-955X](https://orcid.org/0000-0001-5634-955X)

49  
50  
51 **Conflicts of Interest.** The authors declare no conflicts of interest.  
52  
53  
54  
55  
56  
57  
58  
59  
60

1  
2  
3 **Acknowledgments.** This material is based upon work supported by the National Science  
4 Foundation under Grant No. CHE 1710120. V.M. is grateful for financial support from the BMBF  
5 project 05K19PXA. The authors acknowledge Prof. Mark Snyder and Mr. Lohit Sharma for  
6 assistance with obtaining BET data. The authors acknowledge Dr. Martin Etter for his assistance  
7 in acquiring XAS data.  
8  
9  
10  
11  
12  
13  
14  
15  
16  
17  
18  
19  
20  
21  
22  
23  
24  
25  
26  
27  
28  
29  
30  
31  
32  
33  
34  
35  
36  
37  
38  
39  
40  
41  
42  
43  
44  
45  
46  
47  
48  
49  
50  
51  
52  
53  
54  
55  
56  
57  
58  
59  
60

## References

- 1 J. A. Foley, N. Ramankutty, K. A. Brauman, E. S. Cassidy, J. S. Gerber, M. Johnston, N. D. Mueller, C. O'Connell, D. K. Ray, P. C. West, C. Balzer, E. M. Bennett, S. R. Carpenter, J. Hill, C. Monfreda, S. Polasky, J. Rockström, J. Sheehan, S. Siebert, D. Tilman and D. P. M. Zaks, Solutions for a cultivated planet, *Nature*, 2011, **478**, 337.
- 2 J. N. Galloway, J. D. Aber, J. W. Erisman, S. P. Seitzinger, R. W. Howarth, E. B. Cowling and B. J. Cosby, The Nitrogen Cascade, *Bioscience*, 2003, **53**, 341–356.
- 3 J. N. Galloway and E. B. Cowling, Reactive Nitrogen and The World: 200 Years of Change, *AMBIO A J. Hum. Environ.*, 2002, **31**, 64–71.
- 4 J. N. Galloway, A. R. Townsend, J. W. Erisman, M. Bekunda, Z. Cai, J. R. Freney, L. A. Martinelli, S. P. Seitzinger and M. A. Sutton, Transformation of the Nitrogen Cycle: Recent Trends, Questions, and Potential Solutions, *Science (80-. )*, 2008, **320**, 889–892.
- 5 S. Cheng, L. Shao, J. Ma, X. Xia, Y. Liu, Z. Yang, C. Yang and S. Li, Simultaneous removal of phosphates and dyes by Al-doped iron oxide decorated MgAl layered double hydroxide nanoflakes, *Environ. Sci. Nano*, 2019, **6**, 2615–2625.
- 6 J. J. Beaulieu, T. DelSontro and J. A. Downing, Eutrophication will increase methane emissions from lakes and impoundments during the 21st century, *Nat. Commun.*, , DOI:10.1038/s41467-019-09100-5.
- 7 T. Cai, S. Y. Park and Y. Li, Nutrient recovery from wastewater streams by microalgae: Status and prospects, *Renew. Sustain. Energy Rev.*, 2013, **19**, 360–369.
- 8 M. I. H. Bhuiyan, D. S. Mavinic and R. D. Beckie, A solubility and thermodynamic study of struvite, *Environ. Technol.*, 2007, **28**, 1015–1026.
- 9 K. S. Le Corre, E. Valsami-Jones, P. Hobbs and S. A. Parsons, Phosphorus Recovery from Wastewater by Struvite Crystallization: A Review, *Crit. Rev. Environ. Sci. Technol.*, 2009, **39**, 433–477.
- 10 M. M. Rahman, M. A. M. Salleh, U. Rashid, A. Ahsan, M. M. Hossain and C. S. Ra, Production of slow release crystal fertilizer from wastewaters through struvite crystallization -- A review, *Arab. J. Chem.*, 2014, **7**, 139–155.
- 11 I. S. A. I. Mutaz and K. M. Wagialia, Production of magnesium from desalination brines, *Resour. Conserv. Recycl.*, 1990, **3**, 231–239.
- 12 J. Liu, M. D. Bearden, C. A. Fernandez, L. S. Fifield, S. K. Nune, R. K. Motkuri, P. K. Koech and B. P. McGrail, Techno-Economic Analysis of Magnesium Extraction from Seawater via a Catalyzed Organo-Metathetical Process, *Jom*, 2018, **70**, 431–435.
- 13 D. Kiani, Y. Sheng, B. Lu, D. Barauskas, K. Honer, Z. Jiang and J. Baltrusaitis, Transient Struvite Formation during Stoichiometric (1:1) NH<sub>4</sub><sup>+</sup> and PO<sub>4</sub><sup>3-</sup> Adsorption/Reaction on Magnesium Oxide (MgO) Particles, *ACS Sustain. Chem. Eng.*, 2018, **7**, 1545–1556.
- 14 P. Xia, X. Wang, X. Wang, J. Song, H. Wang and J. Zhang, Struvite crystallization

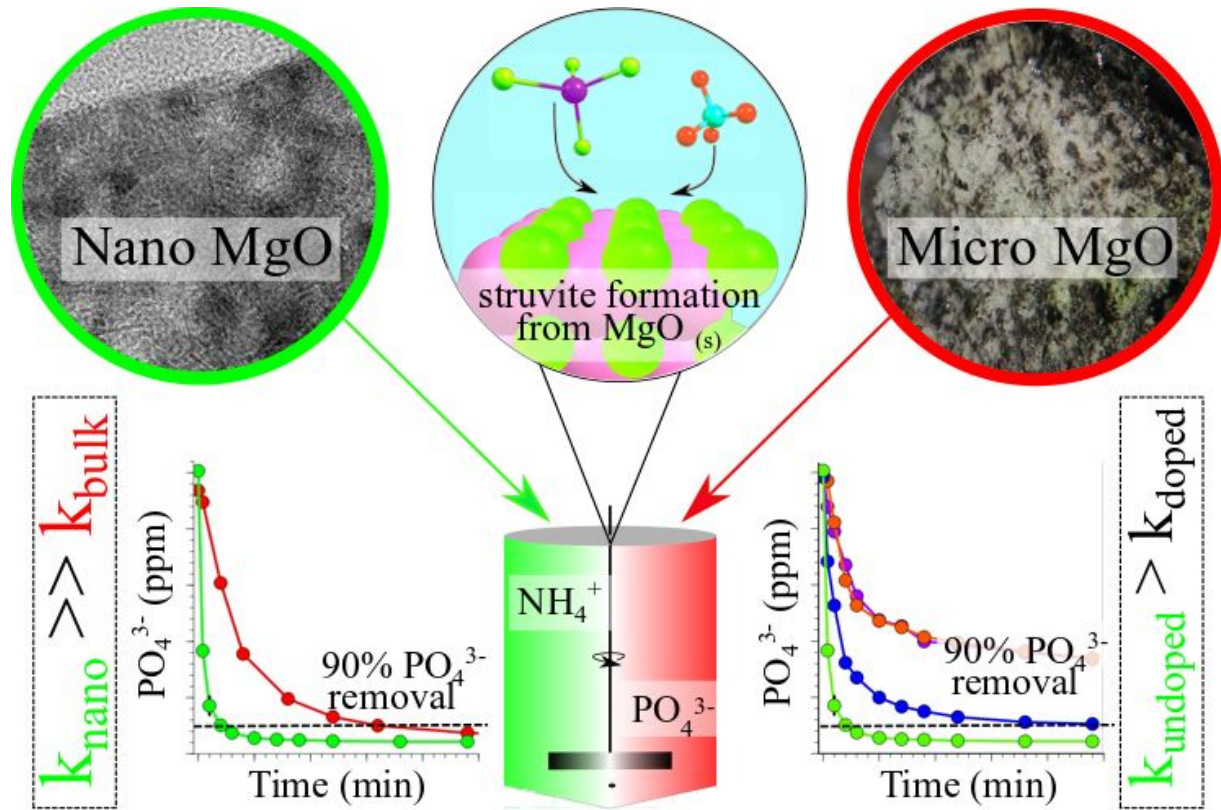
- combined adsorption of phosphate and ammonium from aqueous solutions by mesoporous MgO-loaded diatomite, *Colloids Surfaces A Physicochem. Eng. Asp.*, 2016, **506**, 220–227.
- 15 M. Quintana, M. F. Colmenarejo, J. Barrera, G. García, E. García and A. Bustos, Use of a Byproduct of Magnesium Oxide Production To Precipitate Phosphorus and Nitrogen as Struvite from Wastewater Treatment Liquors, *J. Agric. Food Chem.*, 2004, **52**, 294–299.
- 16 M. Quintana, E. Sánchez, M. F. Colmenarejo, J. Barrera, G. García and R. Borja, Kinetics of phosphorus removal and struvite formation by the utilization of by-product of magnesium oxide production, *Chem. Eng. J.*, 2005, **111**, 45–52.
- 17 J. Li, X. Wang, J. Wang, Y. Li, S. Xia and J. Zhao, Simultaneous recovery of microalgae, ammonium and phosphate from simulated wastewater by MgO modified diatomite, *Chem. Eng. J.*, 2019, **362**, 802–811.
- 18 B. Lu, D. Kiani, W. Taifan, D. Barauskas, K. Honer, L. Zhang and J. Baltrusaitis, Spatially Resolved Product Speciation during Struvite Synthesis from Magnesite ( $\text{MgCO}_3$ ) Particles in Ammonium ( $\text{NH}_4^+$ ) and Phosphate ( $\text{PO}_4^{3-}$ ) Aqueous Solutions, *J. Phys. Chem. C*, 2019, **123**, acs.jpcc.8b12252.
- 19 E. Kirinovic, A. R. Leichtfuss, C. Navizaga, H. Zhang, J. D. S. Christus and J. Baltrusaitis, Spectroscopic and microscopic identification of the reaction products and intermediates during the struvite ( $\text{MgNH}_4\text{PO}_4 \cdot 6\text{H}_2\text{O}$ ) formation from magnesium oxide (MgO) and magnesium carbonate ( $\text{MgCO}_3$ ) microparticles, *ACS Sustain. Chem. Eng.*, 2017, **5**, 1567–1577.
- 20 J. Hövelmann and C. V. Putnis, In Situ nanoscale imaging of struvite formation during the dissolution of natural brucite: Implications for phosphorus recovery from wastewaters, *Environ. Sci. Technol.*, 2016, **50**, 13032–13041.
- 21 D. Kiani, M. Silva, Y. Sheng and J. Baltrusaitis, Experimental Insights into the Genesis and Growth of Struvite Particles on Low-Solubility Dolomite Mineral Surfaces, *J. Phys. Chem. C*, , DOI:10.1021/acs.jpcc.9b05292.
- 22 J. Pesonen, P. Myllymäki, S. Tuomikoski, G. Vervecken, T. Hu, H. Prokkola, P. Tynjälä, U. Lassi, J. Pesonen, P. Myllymäki, S. Tuomikoski, G. Vervecken, T. Hu, H. Prokkola, P. Tynjälä and U. Lassi, Use of Calcined Dolomite as Chemical Precipitant in the Simultaneous Removal of Ammonium and Phosphate from Synthetic Wastewater and from Agricultural Sludge, *ChemEngineering*, 2019, **3**, 40.
- 23 L. Chen, C. H. Zhou, H. Zhang, D. S. Tong, W. H. Yu, H. M. Yang and M. Q. Chu, Capture and recycling of ammonium by dolomite-aided struvite precipitation and thermolysis, *Chemosphere*, 2017, **187**, 302–310.
- 24 M. A. Barakat, *Arab. J. Chem.*, 2011, **4**, 361–377.
- 25 C. Tang, Z. Liu, C. Peng, L. Y. Chai, K. Kuroda, M. Okido and Y. X. Song, New insights into the interaction between heavy metals and struvite: Struvite as platform for heterogeneous nucleation of heavy metal hydroxide, *Chem. Eng. J.*, 2019, **365**, 60–69.
- 26 A. A. Rouff, M. V. Ramlogan and A. Rabinovich, Synergistic Removal of Zinc and

- 1  
2  
3  
4  
5  
6  
7  
8  
9  
10  
11  
12  
13  
14  
15  
16  
17  
18  
19  
20  
21  
22  
23  
24  
25  
26  
27  
28  
29  
30  
31  
32  
33  
34  
35  
36  
37  
38  
39  
40  
41  
42  
43  
44  
45  
46  
47  
48  
49  
50  
51  
52  
53  
54  
55  
56  
57  
58  
59  
60
- Copper in Greenhouse Waste Effluent by Struvite, *ACS Sustain. Chem. Eng.*, 2016, **4**, 1319–1327.
- 27 A. A. Rouff and K. M. Juarez, Zinc Interaction with Struvite During and After Mineral Formation, *Environ. Sci. Technol.*, 2014, **48**, 6342–6349.
- 28 M. Ronteltap, M. Maurer and W. Gujer, The behaviour of pharmaceuticals and heavy metals during struvite precipitation in urine, *Water Res.*, 2007, **41**, 1859–1868.
- 29 A. Uysal, Y. D. Yilmazel and G. N. Demirer, The determination of fertilizer quality of the formed struvite from effluent of a sewage sludge anaerobic digester, *J. Hazard. Mater.*, 2010, **181**, 248–254.
- 30 W. A. Deer, R. A. Howie and J. Zussman, *An Introduction to the Rock-Forming Minerals*, Mineralogical Society of Great Britain and Ireland, 2013.
- 31 P. Raschman and A. Fedoročková, Dissolution kinetics of periclase in dilute hydrochloric acid, *Chem. Eng. Sci.*, 2008, **63**, 576–586.
- 32 N. Z. Janković and D. L. Plata, Engineered nanomaterials in the context of global element cycles, *Environ. Sci. Nano*, 2019, **6**, 2697–2711.
- 33 F. Demir, O. Laçın and B. Dönmez, Leaching kinetics of calcined magnesite in citric acid solutions, *Ind. Eng. Chem. Res.*, 2006, **45**, 1307–1311.
- 34 J. Baltrusaitis, C. Hatch and R. Orlando, Periodic DFT study of acidic trace atmospheric gas molecule adsorption on Ca- and Fe-doped MgO(001) surface basic sites, *J. Phys. Chem. A*, 2012, **116**, 7950–7958.
- 35 S. W. Bian, J. Baltrusaitis, P. Galhotra and V. H. Grassian, A template-free, thermal decomposition method to synthesize mesoporous MgO with a nanocrystalline framework and its application in carbon dioxide adsorption, *J. Mater. Chem.*, 2010, **20**, 8705–8710.
- 36 P. Stolzenburg, A. Capdevielle, S. Teychené and B. Biscans, Struvite precipitation with MgO as a precursor: Application to wastewater treatment, *Chem. Eng. Sci.*, 2014, **133**, 9–15.
- 37 S. K. L. Ishii and T. H. Boyer, Life cycle comparison of centralized wastewater treatment and urine source separation with struvite precipitation: Focus on urine nutrient management, *Water Res.*, 2015, **79**, 88–103.
- 38 K. Yetilmezsoy and Z. Sapci-Zengin, Recovery of ammonium nitrogen from the effluent of UASB treating poultry manure wastewater by MAP precipitation as a slow release fertilizer, *J. Hazard. Mater.*, 2009, **166**, 260–269.
- 39 T. Zhang, L. Ding and H. Ren, Pretreatment of ammonium removal from landfill leachate by chemical precipitation, *J. Hazard. Mater.*, 2009, **166**, 911–915.
- 40 B. Ravel and M. Newville, in *Journal of Synchrotron Radiation*, 2005, vol. 12, pp. 537–541.
- 41 M. Newville, EXAFS analysis using FEFF and FEFFIT, *J. Synchrotron Radiat.*, 2001, **8**, 96–100.

- 1  
2  
3 42 A. Ankudinov and J. Rehr, Relativistic calculations of spin-dependent x-ray-absorption  
4 spectra, *Phys. Rev. B - Condens. Matter Mater. Phys.*, 1997, **56**, R1712–R1716.  
5  
6 43 Y. S. Ho and G. McKay, Pseudo-second order model for sorption processes, *Process*  
7 *Biochem.*, 1999, **34**, 451–465.  
8  
9 44 W. J. Weber and J. C. Morris, Kinetics of Adsorption on Carbon from Solution, *J. Sanit.*  
10 *Eng. Div.*, 1963, **89**, 31–60.  
11  
12 45 R. M. Hazen, *Effects of temperature and pressure on the cell dimension and X-ray*  
13 *temperature factors of periclase*, 1976, vol. 61.  
14  
15 46 M. A. Bañares and I. E. Wachs, in *Encyclopedia of Analytical Chemistry*, John Wiley &  
16 Sons, Ltd, Chichester, UK, 2010.  
17  
18 47 M. Thommes, K. Kaneko, A. V. Neimark, J. P. Olivier, F. Rodriguez-Reinoso, J.  
19 Rouquerol and K. S. W. Sing, Physisorption of gases, with special reference to the  
20 evaluation of surface area and pore size distribution (IUPAC Technical Report), *Pure*  
21 *Appl. Chem.*, 2015, **87**, 1051–1069.  
22  
23 48 F. Meshkani and M. Rezaei, Facile synthesis of nanocrystalline magnesium oxide with  
24 high surface area, *Powder Technol.*, 2009, **196**, 85–88.  
25  
26 49 Z. Zhang, X. Fu, M. Mao, Q. Yu, S. X. Mao, J. Li and Z. Zhang, In situ observation of  
27 sublimation-enhanced magnesium oxidation at elevated temperature, *Nano Res.*, 2016, **9**,  
28 2796–2802.  
29  
30 50 B. Eckhardt, E. Ortel, J. Polte, D. Bernsmeier, O. Görke, P. Strasser and R. Kraehnert,  
31 Micelle-templated mesoporous films of magnesium carbonate and magnesium oxide, *Adv.*  
32 *Mater.*, 2012, **24**, 3115–3119.  
33  
34 51 F. Khairallah, A. Glisenti, A. Galenda and M. M. Natile, Mixed Magnesium and Zinc  
35 Oxide Prepared by Co-precipitation and Analyzed by XPS, *Surf. Sci. Spectra*, 2012, **19**,  
36 13–22.  
37  
38 52 P. S. Wehner, P. N. Mercer and G. Apai, Interaction of H<sub>2</sub> and CO with Rh<sub>4</sub>(CO)<sub>12</sub>  
39 supported on ZnO, *J. Catal.*, 1983, **84**, 244–247.  
40  
41 53 F. Khairallah, A. Glisenti, M. M. Natile and A. Galenda, CuO/MgO Nanocomposites by  
42 Wet Impregnation: An XPS Study, *Surf. Sci. Spectra*, 2012, **19**, 23–29.  
43  
44 54 N. S. McIntyre and D. G. Zetaruk, X-ray Photoelectron Spectroscopic Studies of Iron  
45 Oxides, *Anal. Chem.*, 1977, **49**, 1521–1529.  
46  
47 55 J. Fan, Z. Zhao, Z. Ding and J. Liu, Synthesis of different crystallographic FeOOH  
48 catalysts for peroxymonosulfate activation towards organic matter degradation, *RSC Adv.*,  
49 2018, **8**, 7269–7279.  
50  
51 56 C. Angelici, F. Meirer, A. M. J. Van Der Eerden, H. L. Schaink, A. Goryachev, J. P.  
52 Hofmann, E. J. M. Hensen, B. M. Weckhuysen and P. C. A. Bruijninx, Ex Situ and  
53 Operando Studies on the Role of Copper in Cu-Promoted SiO<sub>2</sub>-MgO Catalysts for the  
54 Lebedev Ethanol-to-Butadiene Process, *ACS Catal.*, 2015, **5**, 6005–6015.  
55  
56  
57  
58  
59  
60

- 1  
2  
3 57 W. E. Taifan, Y. Li, J. P. Baltrus, L. Zhang, A. I. Frenkel and J. Baltrusaitis, Operando  
4 Structure Determination of Cu and Zn on Supported MgO/SiO<sub>2</sub> Catalysts during Ethanol  
5 Conversion to 1,3-Butadiene, *ACS Catal.*, 2019, **9**, 269–285.  
6  
7 58 K. Asakura and Y. Iwasawa, A structure model as the origin of catalytic properties of  
8 metal-doped MgO systems, *Mater. Chem. Phys.*, 1988, **18**, 499–512.  
9  
10 59 S. Colonna, F. Arciprete, A. Balzarotti, M. Fanfoni, M. De Crescenzi and S. Mobilio, In  
11 situ X-ray absorption measurements of the Cu/MgO(0 0 1) interface, *Surf. Sci.*, 2002, **512**,  
12 L341–L345.  
13  
14 60 J. H. Choy, D. K. Kim, S. H. Hwang and G. Demazeau, Cu K-edge x-ray-absorption  
15 spectroscopic study on the octahedrally coordinated trivalent copper in the perovskite-  
16 related compounds La<sub>2</sub>Li<sub>0.5</sub>Cu<sub>0.5</sub>O<sub>4</sub> and LaCuO<sub>3</sub>, *Phys. Rev. B*, 1994, **50**, 16631–  
17 16639.  
18  
19 61 M. Wilke, O. Hahn, A. B. Woodland and K. Rickers, The oxidation state of iron  
20 determined by Fe K-edge XANES -application to iron gall ink in historical manuscripts, *J.*  
21 *Anal. At. Spectrom.*, 2009, **24**, 1364–1372.  
22  
23 62 A. Kuzmin and J. Chaboy, EXAFS and XANES analysis of oxides at the nanoscale,  
24 *IUCrJ*, 2014, **1**, 571–589.  
25  
26 63 O. L. G. Alderman, M. C. Wilding, A. Tamalonis, S. Sendelbach, S. M. Heald, C. J.  
27 Benmore, C. E. Johnson, J. A. Johnson, H. Y. Hah and J. K. R. Weber, Iron K-edge X-ray  
28 absorption near-edge structure spectroscopy of aerodynamically levitated silicate melts  
29 and glasses, *Chem. Geol.*, 2017, **453**, 169–185.  
30  
31 64 J. N. Harvey, Springer, Berlin, Heidelberg, 2004, pp. 151–184.  
32  
33 65 L. Galois, L. Cormier, G. Calas and V. Briois, Environment of Ni, Co and Zn in low  
34 alkali borate glasses: Information from EXAFS and XANES spectra, *J. Non. Cryst. Solids*,  
35 2001, **293–295**, 105–111.  
36  
37 66 H. C. Wang, Y. L. Wei, Y. W. Yang and J. F. Lee, in *Journal of Electron Spectroscopy*  
38 *and Related Phenomena*, 2005, vol. 144–147, pp. 817–819.  
39  
40 67 R. A. Kelly, J. C. Andrews and J. G. DeWitt, An X-ray absorption spectroscopic  
41 investigation of the nature of the zinc complex accumulated in *Datura innoxia* plant tissue  
42 culture, *Microchem. J.*, 2002, **71**, 231–245.  
43  
44 68 M. C. Hsiao, H. P. Wang and Y. W. Yang, EXAFS and XANES studies of copper in a  
45 solidified fly ash, *Environ. Sci. Technol.*, 2001, **35**, 2532–2535.  
46  
47 69 S. Azizian, Kinetic models of sorption: A theoretical analysis, *J. Colloid Interface Sci.*,  
48 2004, **276**, 47–52.  
49  
50 70 R. Kh Khamizov, D. A. Sveshnikova, A. E. Kucherova and L. A. Sinyaeva, Kinetic  
51 Models of Batch Sorption in a Limited Volume, *Russ. J. Phys. Chem. A*, 2018, **92**, 1451–  
52 1460.  
53  
54 71 D. A. Almasri, N. B. Saleh, M. A. Atieh, G. McKay and S. Ahzi, Adsorption of phosphate  
55  
56  
57  
58  
59  
60

- 1  
2  
3 on iron oxide doped halloysite nanotubes, *Sci. Rep.*, , DOI:10.1038/s41598-019-39035-2.  
4  
5 72 V. Halleux, *EU fertilising products*, 2019.  
6  
7 73 O. US EPA, Agriculture Nutrient Management and Fertilizer.  
8  
9 74 S. W. Gaarenstroom and N. Winograd, Initial and final state effects in the ESCA spectra  
10 of cadmium and silver oxides, *J. Chem. Phys.*, 1977, **67**, 3500–3506.  
11  
12 75 J. G. Jolley, G. G. Geesey, M. R. Hankins, R. B. Wright and P. L. Wichlacz, Auger  
13 electron and X-ray photoelectron spectroscopic study of the biocorrosion of copper by  
14 alginate acid polysaccharide, *Appl. Surf. Sci.*, 1989, **37**, 469–480.  
15  
16 76 T. M. Ivanova, K. I. Maslakov, A. A. Sidorov, M. A. Kiskin, R. V. Linko, S. V. Savilov,  
17 V. V. Lunin and I. L. Eremenko, XPS detection of unusual Cu(II) to Cu(I) transition on  
18 the surface of complexes with redox-active ligands, *J. Electron Spectros. Relat.*  
19 *Phenomena*, 2020, **238**, 146878.  
20  
21 77 Y. Wang and P. M. A. Sherwood, Iron (III) Phosphate (FePO<sub>4</sub>) by XPS, *Surf. Sci.*  
22 *Spectra*, 2002, **9**, 99–105.  
23  
24 78 Y. Wang, D. J. Asunskis and P. M. A. Sherwood, Iron (II) Phosphate (Fe<sub>3</sub>(PO<sub>4</sub>)<sub>2</sub>) by  
25 XPS, *Surf. Sci. Spectra*, 2002, **9**, 91–98.  
26  
27 79 K. N. Kuki, M. A. Oliva and A. C. Costa, The simulated effects of iron dust and acidity  
28 during the early stages of establishment of two coastal plant species, *Water. Air. Soil*  
29 *Pollut.*, 2009, **196**, 287–295.  
30  
31 80 I. Cakmak, Possible roles of zinc in protecting plant cells from damage by reactive oxygen  
32 species, *New Phytol.*, 2000, **146**, 185–205.  
33  
34 81 B. J. Alloway, in *Environmental Geochemistry and Health*, 2009, vol. 31, pp. 537–548.  
35  
36 82 N. K. Fageria, C. Baligar and R. B. Clark, *Adv. Agron.*, 2002, **77**, 185–268.  
37  
38  
39  
40  
41  
42  
43  
44  
45  
46  
47  
48  
49  
50  
51  
52  
53  
54  
55  
56  
57  
58  
59  
60



Nanostructured MgO doped with transition metals have been used to recycled nutrients from wastewater via struvite crystallization.